SARS-CoV-2 Airway Infection Results in Time-dependent Sensory Abnormalities in a Hamster Model

One Sentence Summary**:** SARS-CoV-2 infection results in an interferon-associated transcriptional response in sensory tissues underlying time-dependent hypersensitivity.

Randal A. Serafini[a*], Justin J. Frere[b,c*], Jeffrey Zimering[a,d], Ilinca M. Giosan[a], Kerri D. Pryce[a], Ilona Golynker[c], Maryline Panis[c], Anne Ruiz[a], Benjamin tenOever[c°], Venetia Zachariou[a,e°]

[a] Nash Department of Neuroscience and Friedman Brain Institute, Icahn School of Medicine at Mount Sinai, One Gustave L. Levy Place Box #1022, New York, NY, 10029

[b] Department of Microbiology, Icahn School of Medicine at Mount Sinai, One Gustave L. Levy Place, Box #1124, New York, NY, 10029

[c] Department of Microbiology, New York University Langone, 430-450 E. 29th St., New York, NY 10016

[d] Department of Neurosurgery, Icahn School of Medicine at Mount Sinai, One Gustave L. Levy Place, Box #1136, New York, NY, 10029

[e] Department of Pharmacological Sciences, Icahn School of Medicine at Mount Sinai, One Gustave L. Levy Place Box #1677, New York, New York 10029

*These authors contributed equally to this work.

°Corresponding authors: Benjamin.tenOever@nyulangone.org, venetia.zachariou@mssm.edu

ABSTRACT

Despite being largely confined to the airways, SARS-CoV-2 infection has been associated with sensory abnormalities that manifest in both acute and long-lasting phenotypes. To gain insight on the molecular basis of these sensory abnormalities, we used the golden hamster infection model to characterize the effects of SARS-CoV-2 versus Influenza A virus (IAV) infection on the sensory nervous system. Efforts to detect the presence of virus in the cervical/thoracic spinal cord and dorsal root ganglia (DRGs) demonstrated detectable levels of SARS-CoV-2 by quantitative PCR and RNAscope uniquely within the first 24 hours of infection. SARS-CoV-2-infected hamsters demonstrated mechanical hypersensitivity during acute infection; intriguingly, this hypersensitivity was milder, but prolonged when compared to IAV-infected hamsters. RNA sequencing (RNA-seq) of thoracic DRGs from acute infection revealed predominantly neuron-biased signaling perturbations in SARS-CoV-2-infected animals as opposed to type I interferon signaling in tissue derived from IAV-infected animals. RNA-seq of 31dpi thoracic DRGs from SARS-CoV-2-infected animals highlighted a uniquely neuropathic transcriptomic landscape, which was consistent with substantial SARS-CoV-2-specific mechanical hypersensitivity at 28dpi. Ontology analysis of 1, 4, and 30dpi RNA-seq revealed novel targets for pain management, such as ILF3. Meta-analysis of all SARS-CoV-2 RNA-seq timepoints against preclinical pain model datasets highlighted both conserved and unique pro-nociceptive gene expression changes following infection. Overall, this work elucidates novel transcriptomic signatures triggered by SARS-CoV-2 that may underlie both short- and long-term sensory abnormalities while also highlighting several therapeutic targets for alleviation of infection-induced hypersensitivity.

INTRODUCTION

COVID-19, the disease resulting from SARS-CoV-2 infection, is associated with highly variable clinical outcomes that range from asymptomatic disease to death. For milder infections, COVID-19 is associated with primarily respiratory infection-associated symptoms (cough, congestion, fever) and sensory phenotypes such as headache and anosmia *(1–3)*. For more severe cases, however, SARS-CoV-2 infection has been seen to induce a variety of systemic perturbations that have the ability to affect nearly every organ, including strokes from vascular occlusion, cardiovascular damage, and acute renal failure *(4–6)*. Intriguingly, recent research has shown that a significant number of actively infected patients suffering from both mild and severe infections experience sensory-related symptoms such as headache, visceral pain, Guillain-Barre syndrome (GBS), nerve pain, and polyneuritis *(7–9)*. While these symptoms subside after clearance of infection in a majority of patients, they have been noted to arise in or persist to sub-acute or chronic timepoints for many *(10, 11)*. Sensory-related symptomology is thus a major component of long COVID, a condition defined by the World Health Organization as the persistence of COVID-19-associated symptomology that lasts for at least two months and cannot be explained by an alternative diagnosis *(12)*. Accordingly, high persistence of abdominal, chest, and muscle pains, as well as headaches, was observed in long COVID patients *(13–15)*. Of note, the medical field has observed a high prevalence of asymptomatic acute COVID-19 cases, suggesting a mechanistic divergence between the acute and chronic stages of the disease *(16, 17)*.

Abnormal somatosensation is a common symptom of neuroinvasive and non-neuroinvasive viral infections, including varicella-zoster virus (VZV), human immunodeficiency virus (HIV), and SARS-CoV-2 *(18–20)*. Phenotypes generally consist of painful sensations (burning, prickling, or aching), as well as paresthesias (tingling) or in some cases hypoesthesias

(numbness). The mechanisms underlying these symptoms vary by virus. For example, certain neurotropic viruses, such as herpesviruses, persist in the dorsal root ganglia (DRGs) and directly induce abnormal activity in these primary sensory cells upon reactivation *(21, 22)*. Retroviruses, such as HIV, can induce primary sensory neuropathy through viral protein interaction with axons, while also inducing secondary inflammation at these neural sites, thereby inducing hyperexcitability and chronic pain symptoms *(23, 24)*. However, the mechanisms by which coronaviruses, and specifically SARS-CoV-2, induce abnormal sensation are more poorly understood *(25)*.

The ability of SARS-CoV-2 to pass the blood brain barrier and directly infect the central nervous system (CNS) is currently unclear. While ultrastructural analyses of post-mortem tissue from COVID-19 patients have identified structures resembling viral particles in the central nervous system, other studies have failed to detect replication-competent virus in the brain *(26–30)*. These seemingly disparate results may be explained by pre-clinical studies in the golden hamster model of SARS-CoV-2 infection, which demonstrate the presence of viral RNA in various brain regions, including the olfactory bulb, cortical areas, brainstem, and cerebellum during acute infection, despite lacking evidence for any infectious material *(31, 32)*. Together, these data suggest that virus replication in the airways results in the dissemination of viral RNA and the induction of an antiviral transcriptional response in distal tissues, including the brain, which may underly CNS-related pathologies, such as demyelinating lesions and brain hemopathologies, observed among COVID-19 patients *(33–36)*.

Despite the large number of studies investigating CNS infiltration during SARS-CoV-2 infection, little clinical or pre-clinical literature has investigated penetration capabilities of SARS-CoV-2 into the peripheral nervous system, particularly sensory components such as the dorsal root ganglia (DRGs) and spinal cord (SC). While several case studies have highlighted peripheral fiber neuropathies in actively and recovered COVID-19 patients *(37, 38)*, there is

97 conflicting data regarding the presence of viral transcripts in the cerebrospinal fluid of COVID-19
98 patients *(39–42)*.

99 Previous work with other members of the coronavirus family, including hemagglutinating
100 encephalomyelitis virus (HEV), has identified active replication and satellite-mediated
101 sequestration of virus in rodent DRGs *(43)*. Mouse hepatitis virus also demonstrates anterior
102 spinal cord segment invasion and persistence through neuroanatomical pathways such as the
103 olfactory bulb and trigeminal ganglia, leading to consequences such as demyelination *(44, 45)*.
104 In these studies, the source of coronavirus-induced neurological dysfunction was linked to two
105 major causes: direct virus-induced damage and collateral damage to host cells by anti-viral
106 immune responses *(46, 47)*. While the cause of SARS-CoV-2-linked sensory pathologies is
107 unknown, SARS-CoV-2 has been shown to infect human neuronal cells *in vitro (48, 49)* and to
108 induce a robust *in vivo* systemic inflammatory response *(31, 32)*. Both findings could present
109 causal mechanisms underlying SARS-CoV-2-linked sensory symptoms.

110 We hypothesized that clinically-observed sensory symptoms (both positive and negative)
111 arise from exposure of neurons in the DRG and/or spinal cord to mature virus and/or through
112 circulating inflammatory materials including both cytokines and pathogen-associated molecular
113 patterns (PAMPs). In order to test this hypothesis, we used the Syrian golden hamster model of
114 SARS-CoV-2 respiratory infection, which can accurately phenocopy COVID-19 in the absence
115 of any virus or host adaptation *(31, 32, 50)*. To this end, we used gene/protein quantification and
116 imaging techniques to assess the presence of SARS-CoV-2 in sensory tissues at acute
117 timepoints in cervical and thoracic levels using gene and protein quantification and imaging
118 techniques. We also applied the Von Frey assay to characterize SARS-CoV-2-induced changes
119 in mechanical hypersensitivity compared to mock and IAV-infected hamsters at acute and
120 chronic timepoints. Moreover, in an effort to better define the molecular underpinnings of virus-
121 induced changes in sensory hypersensitivity, we performed RNA sequencing (RNA-seq) of

thoracic DRGs from infected hamsters at 1, 4, and 31 dpi timepoints. We also used ontological analysis of predicted upstream regulators associated with the sequencing results to identify and validate novel therapeutic targets. Lastly, we performed a meta-analysis of 1, 4, and 31 dpi SARS-CoV-2 thoracic DRG sequencing data against publicly-available DRG datasets from rodent pain models to highlight relevant injury response pathways. Our findings provide insights into the sensory-altering mechanisms induced by respiratory SARS-CoV-2 infection and have the potential to guide the development of novel therapeutics for a variety of pain conditions.

RESULTS

SARS-CoV-2 RNA Infiltrates Thoracic and Cervical DRG and Spinal Cord Tissue

We first sought to determine if SARS-CoV-2 genetic material is present in the sensory nervous system tissues and to investigate if this presence was associated with induction of an antiviral response. To this end, we performed a longitudinal cohort study in which hamsters were treated intranasally with SARS-CoV-2 or PBS (mock-infected). Cervical and thoracic levels of DRGs and spinal cord were harvested at 1, 4, 7, and 14dpi in both groups and assessed for the presence of SARS-CoV-2 subgenomic nucleocapsid protein (*N*) and canonical type-I interferon stimulated gene *Isg15* transcripts via quantitative reverse transcription PCR (RT-qPCR). We found a substantial elevation of *N* transcripts at 1dpi in cervical DRGs (**Figure 1A**; two-way ANOVA interaction $F(3,35)=4.205$, $p=0.0122$; multiple t-tests 1dpi $t=2.698$, $df=13$, $p=0.0183$), cervical SC (**Figure 1B**; two-way ANOVA interaction $F(3,35)=3.809$, $p=0.0189$; multiple t-tests 1dpi $t=2.392$, $df=11$, $p=0.0358$), thoracic DRGs (**Figure 1E**; two-way ANOVA interaction $F(3,36)=3.812$, $p=0.018$; multiple t-tests 1dpi, $t=2.528$, $df=13$, $p=0.0252$), and thoracic SC (**Figure 1F**; two-way ANOVA interaction $F(3,34)=4.266$, $p=0.0116$; multiple t-tests 1dpi $t=3.068$, $df=11$, $p=0.0107$). Viral RNA appeared to be cleared in most samples by 4dpi. *Isg15* mRNA levels, which are generally representative of interferon signaling *(51)*, had similar elevation patterns to those of *N* in cervical DRGs (**Figure 1C**; two-way ANOVA interaction

F(3,35)=3.689, p=0.0208, multiple t-tests 1dpi t=3.152, df=13, p=0.00764; 4dpi t=2.361, df=12, p=0.0360), cervical SC (**Figure 1D**; two-way ANOVA interaction F(3,35)=5.001, p=0.0054; multiple t-tests 1dpi t=6.034, df=12, p=0.0000590; 4dpi t=2.656, df=13, p=0.0198), thoracic DRGs (**Figure 1G**; two-way ANOVA interaction F(3,36)=1.856, p=0.155; multiple t-tests 1dpi t=3.541, df=13, p=0.00362; 4dpi t=2.311, df=13, p=0.0379), and thoracic SCs (**Figure 1H**; two-way ANOVA interaction F(3,35)=8.478, p=0.0002; multiple t-tests 1dpi t=4.286, df=12, p=0.00106; 4dpi t=3.333, df=13, p=0.00539).

In order to gain insight into viral replication within the DRG, we performed a plaque assay in which combined cervical and thoracic DRGs or SC were collected at 3dpi and homogenized in PBS. This solution was then plated with Vero cells, with the number of ensuing plaques representing the number of mature virions present in the harvested tissue. As seen in **Figure 1I**, plaques were observed only in 3dpi lung homogenate from SARS-CoV-2-infected animals, but not in mock lung or any DRG or SC tissue. This suggested that mature virus was not reaching the peripheral or central sensory nervous systems.

We next sought to determine whether SARS-CoV-2 transcripts were localized to specific cell types in the DRG, which is predominantly composed of primary sensory neurons and satellite glial cells. By using RNAscope *in situ* hybridization on 1dpi cervical and thoracic cell tissue, we observed the presence of RNA (*S*) puncta around DAPI-labeled nuclei, which in DRGs are representative of satellite glial cells and *Rbfox3*-labeled neuronal spaces, but not in mock samples (**Figure 2A**). We also detected *S* transcript puncta near DAPI signal throughout SARS-CoV-2-infected cervical and thoracic spinal cord sections on 1dpi, but not in mock samples **(Figure 2B**).

Of note, when tissue sections obtained from the DRGs of SVC2- or mock-infected hamsters were immuno-labeled for SARS-CoV-2 nucleocapsid protein (NP) we did not observe any notable viral protein presence **(Figure 2C)**. Importantly, we confirmed the presence of NP in

SARS-CoV-2-infected lung samples, but not in mock controls **(Figure 2C)**. This introduced the question of whether the presence of viral mRNA and associated antiviral response signatures in the sensory nervous system are sufficient to induce behavioral and/or transcriptional perturbations.

SARS-CoV-2 and IAV Induce Unique Mechanical Hypersensitivity Signatures

We next sought to determine whether the presence of SARS-CoV-2 RNA or associated type I interferon (IFN-I) signaling, as reported previously *(52)*, was associated with the induction of sensory hypersensitivity. To assess this, we performed the Von Frey assay on hamsters infected with either IAV (A/California/04/2009) or SARS-CoV-2. IAV, similar to SARS-CoV-2, is an RNA virus of the respiratory tract that is known to provoke a systemic inflammatory response similar to SARS-CoV-2, resulting in clinically-associated myalgias *(32, 53)*. Von Frey thresholds were measured during the acute phase of infection (1 and 4dpi) to identify the effects of active and subsiding SARS-CoV-2 mRNA presence and IFN-I response on sensation. As seen in **Figure 3A,** we observed a significant interaction effect between time and virus on mechanical hypersensitivity (RM two-way ANOVA Interaction $F(4,18)=4.16$, df=4, $p=0.0147$). IAV induced robust hypersensitivity at 1dpi which completely subsided by 4dpi (one-way ANOVA $F=6.092$, $p=0.0359$; Tukey's m.c.: Baseline vs. 1dpi $q=4.604$, df=6, $p=0.0398$). SARS-CoV-2 infection instead resulted in a gradual exacerbation of hypersensitivity, reaching significance only at 4dpi (one-way ANOVA $F=9.772$, $p=0.013$; Tukey's m.c.: Baseline vs. 4dpi $q=6.117$, df=6, $p=0.0117$). Importantly, 1dpi IAV-induced hypersensitivity was significantly higher than that caused by 1dpi SARS-CoV-2 (RM two-way ANOVA Tukey's m.c. $q=4.033$, df=27, $p=0.0218$). Considering the emergence of distinct behavioral signatures irrespective of systemic interferon responses induced by these two viruses, we performed a time-dependent transcriptional comparison of sensory structures after infection.

Sensory Transcriptional Response to SARS-CoV-2 Infection

We conducted transcriptional profiling via RNA-seq on thoracic DRGs from SARS-CoV-2- and IAV-infected hamsters at both 1dpi and 4dpi because of their respiratory, visceral, and dermal innervations. Differential expression analysis of RNA-seq data revealed transcriptomic changes in both SARS-CoV-2- and IAV-infected thoracic DRGs compared to mock at 1dpi and 4dpi. SARS-CoV-2 infection resulted in a more robust differential expression at both time points: 344 genes at 1dpi (271 up & 79 down; p-adj.<0.1) and 63 genes at 4dpi (52 up & 11 down; p-adj.<0.1). IAV infection resulted in differential expression of 82 genes at 1dpi (79 up & 3 down; p-adj.<0.1) and 18 genes at 4dpi (9 up & 9 down; p-adj.<0.1) **(Figure 3B)**. Considering the milder acute mechano-sensitivity phenotype in SARS-CoV-2-infected hamsters and greater differential gene expression compared to IAV-infected hamsters, we hypothesized that certain acute SARS-CoV-2-induced transcriptional changes may counteract interferon-induced somatosensory sensitization, potentially by causing a stronger neuronal gene adaptation signature. To better assess this, we performed a canonical pathway analysis (IPA, Qiagen) on our RNA-seq data. This analysis showed neuron-specific transcriptional differences within the reported top upregulated canonical pathways (based on genes with nominal p<0.05) **(Figure 3C).** The top two most enriched pathways for 1dpi SARS-CoV-2 tissue was “Axonal Guidance Signaling” and “Synaptogenesis Signaling”, and at 4dpi “Neuroinflammation Signaling” was among the top-five pathways. However, for IAV samples, the top canonical pathway results were consistently representative of generic viral response pathways.

To better understand which transcripts were driving these enriched annotations, we compared DEGs (p-adj.<0.1) between tissues derived from IAV- and SARS-CoV-2-infected hamsters. Commonly upregulated genes between 1dpi and 4dpi SARS-CoV-2 and IAV tissues were primarily anti-viral in nature, with only one co-downregulated gene emerging at 4dpi, *Svep1* (a vascular gene whose locus has been associated with poor SARS-CoV-2 clinical outcomes *(54)*) **(Figure 3D).** RNA-seq was validated at 1dpi and 4dpi through qPCR

measurement of neuronal and anti-viral genes from SARS-CoV-2 and mock tissues. Interestingly, we observed bi-directional regulation of neuropathy-associated and/or pro-nociceptive genes at 1dpi, such as upregulation of *Sema3b (55) and Vegfa (56, 57)* and downregulation of *Rgs4 (58)* **(Figure 3E)**. qPCR validations of 4dpi included upregulation of *Mx1* and *Irf7* (pro-inflammatory, anti-viral genes) *(59)*, as well as *Slc6a4 (60)* and *Rgs18 (61)*, which have also been implicated in sensory abnormalities **(Figure 3E)**.

Analysis of upstream regulators (URs; IPA, Qiagen) of differentially expressed nominal $p<0.05$ genes on IPA revealed several commonly- and oppositely-regulated URs between SARS-CoV-2 and IAV datasets. Based on our hypothesis that SARS-CoV-2 transcriptionally counteracts interferon-induced hypersensitivity, we wanted to identify URs uniformly associated with timepoints of acute viral infection during which lower levels of hypersensitivity were observed, namely 1dpi SARS-CoV-2, 4dpi SARS-CoV-2, and 4dpi IAV. We focused on URs with predicted downregulated activity in an attempt to find inhibition targets. Nine URs met this criterion: Interleukin 6 Receptor (IL6R), Mitogen-activated Protein Kinase Kinase (MEK), Interleukin Enhancer-binding Factor 3 (ILF3), Runt-related Transcription Factor 2 (RUNX2), Protein Kinase AMP-Activated Catalytic Subunit Alpha 2 (PRKAA2) (UR was AMPKα2 gene), Follicle Stimulating Hormone (FSH), Activating Transcription Factor 4 (ATF4), Snail Family Transcriptional Repressor 1 (SNAI1), and Inhibin Subunit Alpha (INHA) (**Figure 3F**). Interestingly, pre-clinical and clinical literature supports a positive association between upregulation/activation of IL6R *(62–64)*, MEK *(65–67)*, RUNX2 *(68, 69)*, FSH *(70)*, & ATF4 *(71, 72)* and nociceptive states, and several laboratories have validated interventions in relevant pathways as promising anti-nociceptive therapeutic strategies. Only AMPKα2 activity was expressed towards a pro-nociceptive direction in this list, as pre-clinical literature suggests activation of this protein is associated with the alleviation of nociceptive symptoms *(73, 74)*. These data suggest that other targets in this list may serve as novel therapeutic avenues of pain

management. Among the identified genes that have not been studied in pain models (SNAI1, ILF3, and INHA), we selected to study ILF3 as there is a commercially available inhibitor, YM155, which can be systemically applied and has been clinically tested in various cancer subtype populations *(75–77)*.

Predicted interactions between ILF3 and SARS-CoV-2-regulated genes further support its investigation as a pain target, as several genes were associated with either neuronal activity/plasticity (including *Fos, Col14a1, Aldh1a2, Fkbp5, Sema7a, Mgll Chi3l1, and Slc3a2*), or with interferon and cytokine responses (including *Isg15, Il1b, Il1rn, Tlr3, Tnc*) **(Figure 3H)**. As expected based on RNAseq, which did not label *Ilf3* as a significant DEG, whole tissue qPCR demonstrated a lack of *Ilf3* gene expression changes in SARS-CoV-2 and IAV tissues from 1dpi or 4dpi timepoints, suggesting that changes in the activity of this molecule are occurring at the protein level **(Figure 3G).** Of note, YM155 is believed to affect subcellular localization of ILF3 and its associated complexes, as opposed to directly inhibiting its expression *(78)*.

Inhibition of ILF3 Activity Alleviates Sensory Hypersensitivity in an Inflammatory Pain Model

We next used the CFA model of peripheral inflammation in female mice in order to determine the impact of ILF3 inhibition in sensory hypersensitivity behaviors associated with inflammatory pain states. We observed lethal toxicity at 20 mg/kg, so we proceeded with a 5 mg/kg once-daily regimen. In order to identify any immediate analgesic effects of YM155 under local, peripheral inflammation conditions, we first tested CFA-injected mice in the Von Frey and Hargreave's assays at 30 minutes post-drug administration. YM155-treated mice displayed increased Hargreave's response times (**Figure 4A**; RM two-way ANOVA Interaction: $F(2,20)=4.116$, df=2, $p=0.0318$; Sidak's m.c.: YM155 vs Saline D3 Post-CFA (+drug) $t=3.085$, df=30, $p=0.013$; YM155 D2 Post-CFA (-drug) vs D3 Post-CFA (+drug) $t=3.36$, df=20, $p=0.0186$) and increased Von Frey thresholds (**Figure 4B**; RM two-way ANOVA Interaction: $F(2,20)=13.5$, df=2, $p=0.0002$; Sidak's m.c.: YM155 vs Saline Day 4 Post-CFA (+drug) $t=6.784$, df=30,

p<0.0001, YM155 D2 Post-CFA (-drug) vs D4 Post-CFA (+drug) t=8.517, df=20, p<0.0001). We also tested whether YM155 had sustained effects on sensory hypersensitivity after the expected window of activity (approximately 24 hours post-injection, based on a ~one hour half-life in intravenously-treated mice*(79)*). Indeed, when mice were monitored in the Hargreave's assay at 24 hours post-injection, we observed a significantly higher withdrawal latency at six consecutive days (PD-D6) of YM155 administration (**Figure 4C**; RM two-way ANOVA Interaction: F(4,40)=2.887, df=4, p=0.0343; Sidak's m.c.: YM155 vs Saline PD-D6 t=3.964, df=50, p=0.0012), prior to the expected recovery from thermal hypersensitivity in CFA animals. Similarly, we observed sustained recovery of mechanical thresholds on PD-D5, PD-D7, and PD-D9 in the Von Frey assay (**Figure 4D**; RM two-way ANOVA Interaction: F(4,40)=2.171, df=4, p=0.0897; Sidak's m.c.: YM155 vs Saline PD-D5 t=3.59, df=50, p=0.0038; PD-D7 t=3.058, df=50, p=0.0177; PD-D9 t=4.122, df=50, p=0.0007). We observed no changes in weight due to YM155 administration over the first 9 days of treatment (**Figure 4E**).

We also tested whether YM155 could be used to prophylactically reduce pain experienced after acute post-operative injuries. For this, we used the paw incision model and pre-treated animals at a dose of 5mg/kg i.p. for seven days. Animals were not treated with drug after the incision. We observed a significant reduction in mechanical hypersensitivity due to the incision (**Figure 4F**; RM two-way ANOVA Interaction: F(6,60)=2.384, df=6, p=0.0393; Sidak's m.c. YM155 vs Saline t=3.203, df=70, D2 p=0.0142). Importantly, we observed no changes in locomotor activity between animals immediately after testing mechanical hypersensitivity on D1 post-op (**Figure 4G**).

SARS-CoV-2 Induces a Unique, Persistent Transcriptomic Profile in DRGs

Given that the severity of sensory hypersensitivity during acute infection with SARS-CoV-2 worsens over time and the existence of persistent sensory symptoms in patients afflicted by long COVID, we set out to determine whether the hamster respiratory model of SARS-CoV-2

297 infection displayed any prolonged sensory phenotypes. In this set of studies, we monitored
298 mechanical hypersensitivity in male and female SARS-CoV-2, IAV, and mock treated hamsters
299 at 28dpi (well-after viral clearance). Our findings reveal substantial mechanical hypersensitivity
300 in SARS-CoV-2-infected hamsters of both sexes, but normal responses for IAV and mock
301 hamsters **(Figure 5A;** for female groups: one-way ANOVA $F(2,15)=8.469$, $p=0.0035$, Tukey's
302 m.c. SARS-CoV-2vsMock $q=5.385$, $df=15$, $p=0.0046$; SARS-CoV-2vsIAV $q=4.605$, $df=15$,
303 $p=0.0138$; for male groups: one-way ANOVA $F(2,15)=22.36$, $p<0.0001$, Tukey's m.c. SARS-
304 CoV-2vsMock $q=8.043$, $df=15$, $p=0.0001$; SARS-CoV-2vsIAV $q=8.331$, $df=15$, $p<0.0001$).

305 In order to determine whether longitudinally-altered DRG molecular mechanisms may be
306 responsible for this SARS-CoV-2-specific hypersensitivity phenotype, we performed RNA-seq
307 analysis and compared 31dpi thoracic DRGs between SARS-CoV-2 and Mock male animals. To
308 our surprise, we identified 1065 DEGs (p-adj.<0.1, 170 up, 895 down; **Figure 5B**), which is a
309 much larger number of DEGs than we observed with the 4dpi SARS-CoV-2 DRGs. Ontology
310 analysis of DEGs (nominal $p<0.05$) also highlighted new and counter-regulated canonical
311 pathways compared to those observed in 1dpi and 4dpi SARS-CoV-2 and IAV, including
312 decreased "Synaptogenesis Signaling", and the involvement of "EIF2 Signaling", "mTOR
313 Signaling", "Opioid Signaling", and "SNARE Signaling" (**Figure 5C;** $-\log_{10}$(p-value)>1.3**)**.
314 Furthermore, use of Enrichr's DisGeNET gateway primarily associated these DEGs with neuro-
315 oncological and neurodegenerative conditions, including Glioblastoma, Alzheimer's Disease,
316 Parkinson Disease, and Neurilemmoma **(Figure 5D).** Key DEGs (p-adj.<0.1) from RNAseq
317 support our observed maladaptive alterations in canonical neuronal and inflammatory pathways,
318 including changes in gene expression of several tubulin mRNA (*Tubb*) isoforms, myelin
319 proteins, activity-related channels, extracellular matrix proteins, and cytokine/interferon-related
320 proteins **(Figure 5E)**.

Analysis of predicted cell subtype implications influence on 31dpi SARS-CoV-2 tDRG transcriptomic signatures using GSEA (C8 cell type signature gene set (v7.4)) revealed a positive contribution of pro-inflammatory cells, such as B cells, T cells, and dendritic cells **(Figure 5F)**. Astrocytes, microglia, interneurons, and excitatory neurons contributions were negatively enriched **(Figure 5F)**. Overall, these predictions suggest that 31dpi SARS-CoV-2 tDRGs are undergoing a pro-inflammatory state with inhibited neuronal and glial function, which is reflective of the ontology analysis above.

We next sought to determine whether a core group of upstream regulators (URs) may serve as a common target for sensory and perceptive components of pain, as well as affective comorbidities observed in long COVID-19 patients. We performed an IPA UR comparison analysis between our 31dpi DRG, Striatum, and Thalamus RNA-seq data, the latter two datasets coming from another systemic long-COVID study our group performed in hamsters under the same conditions *(32)*. The Striatum and Thalamus are all well-cited regions involved in the initiation and maintenance of sensory components of pain, as well as emotional pain signs, such as catastrophizing *(80, 81)*. Here, we focused on the top common upstream regulators across these regions.

Interestingly, a majority of the top 15 URs demonstrated a unidirectional predicted activation/inhibition state between Thalamus and Striatum, but not DRGs **(Figure 5G)**. However, we did observe a common upregulation of PTPRR and miR17hg, as well as a downregulation of FIRRE, between DRG and Thalamus. While PTPRR, a protein tyrosine phosphatase receptor, has not been implicated in pain, human studies have suggested an association between its upregulation and depression *(82, 83)*. *MIR17HG* (a long non-coding RNA (lncRNA) involved in cell survival) gene abnormalities have also been reported in Feingold 2 syndrome patients that suffer from chronic myofascial pain and affective symptoms *(84, 85)*. FIRRE, another lncRNA, has been implicated in spinal cord neuropathic pain mechanisms *(86)*.

Thus, common regulators between the peripheral and central nervous systems may serve as useful targets for both sensory and affective symptoms of long COVID-19.

SARS-CoV-2 Infection Causes Transcriptomic Signatures Similar to Persistent Inflammation and Nerve Injury Models in Dorsal Root Ganglia

While our bioinformatic analysis of SARS-CoV-2 RNA-seq datasets led to the identification of potential treatment targets, such as ILF3, we also wanted to determine if a meta-analysis of this data against existing injury datasets may yield a more comprehensive list of pain targets. We therefore compared 1, 4, and 31dpi thoracic DRG RNA-seq from SARS-CoV-2-infected hamsters against GEO RNA sequencing data from the aforementioned murine SNI and CFA datasets.

We observed several commonly upregulated genes between SARS-CoV-2 and CFA at both 1 and 4dpi, and only on 1dpi when comparing to SNI **(Figure 6A)**. Interestingly, we identified a group of 53 genes that were upregulated by SARS-CoV-2 at 1dpi but downregulated by SNI (**Figure 6A**). g:Profiler associated this gene set with neuroplasticity, particularly in the synaptic/dendritic cellular compartments, and strongly associated the Sp1 transcription factor (implicated in several pro-nociceptive mechanisms) with these genes **(Figure 6B)** *(87–89)*. Some of these genes, such as *Scn4b (90, 91)*, *Rhobtb2 (92)*, *Mgll (93, 94)*, and *Cntfr (95)* have been positively associated with sensory hypersensitivity under injury states, suggesting they may be unique mechanisms by which SARS-CoV-2 induces mild hypersensitivity. This finding also highlights potential SNI-induced compensatory anti-nociceptive gene programs. However, anti-nociceptive genes were also upregulated by SARS-CoV-2, including *Gprc5b (96)* and *Grk2 (97, 98)*. Several genes implicated in neurodevelopment and dendritic plasticity were also upregulated by SARS-CoV-2, but have not yet been studied in pain. Interesting candidates include *Olfm1, Fxr2, Atcay, Cplx1, Iqsec1, Dnm1, Clstn1, Rph3a, Scrt1, Ntng2* and *Lhfpl4*. Ontologies significantly associated with this SARS-CoV-2 versus SNI contra-regulated gene list

are GO:BP nervous system development (p-adj=0.005994), GO:BP generation of neurons (p-adj=0.024), GO:CC somatodendritic compartment (p-adj=0.004204), GO:CC synapse (p-adj=0.01054), and GO:CC cell junction (p-adj=0.02067). We also identified a core set of genes, mostly associated with extracellular matrix remodeling, was commonly upregulated between 1dpi SARS-CoV-2, CFA, and SNI: *Col1a1, Col1a2, Col6a3, Hspg2, Irgm, Lama2, Lamb1, Lamc1, and Siglec1* **(Figure 6C)**. This is in agreement with previous literature implicating extracellular matrix remodeling with the maintenance of inflammatory- and nerve injury-associated pain sensation *(99)*.

Lastly, comparison of all genes regulated by CFA and 31dpi SARS-CoV-2 revealed a subset of counter-regulated DEGs (36 CFA Up-SARS-CoV-2 down; p-adj.<0.1). These genes are implicated in pathways such as myelination/axon ensheathment (*Mpz, Mbp, Prx, Fa2h, Dhh,* and *Mag*), semaphorin-regulation of axonogenesis (*Sema3g and Sema4g*), and extracellular matrix organization (*Nid2, Col5a3, Mmp15, Mmp14, Col4a1, and Fscn1*) (g:profiler GO:BP p-adj.<0.05). We observed a strong transcriptional counter-regulation between SNI and 31dpi SARS-CoV-2 as well (89 SNI up-SARS-CoV-2 down; p-adj.<0.1). This signature was predominantly related with nervous system development, with implicated genes including *Mpz, Plec, Prkcg Metrn, Slit1, Brd2, Anks1a, Cpne5, Sema4f, Hspg2, Sh3gl1, Prag1, Map6, Mdga1, Fphs, Ppp2r5b, Plod3, Phgdh, Dpysl5, Gpc1, Elavl3, Gpsm1, Marcksl1, Col4a1, Niban2, Carm1, Irs2, Lgi4, Erbb2, Syngap1,* and *Nlgn2* (g:profiler GO:BP p-adj.<0.05).

However, we were mostly surprised by the robust overlap of downregulated DEGs between SNI and 31dpi SARS-CoV-2 (179; p-adj.<0.1). Nervous system development and morphogenesis were robust pathway signatures, implicating neuronal plasticity as a key contributor to nerve injury and virus-induced pain states. But this comparison also uniquely revealed strongly altered synaptic transmission pathways, with DEGs including *Slc7a7, Syngr1, Prkaca, Rab3a, Ntrk1, Nptx1, Stx1b, Jph3, Mapk8ip2, Calm3, Pnkd, Ppp1r9b, Pip5k1c, Cacng7,*

Dlgap3, Nrxn2, Pink1, Grk2, Ncdn, Cplx2, Camk2b, Grin1, Brsk1, Ache, and *Jph4*. This gene list suggests that SARS-CoV-2 mirrors nerve injury maladaptive mechanisms both through direct modification of neuronal excitability at the membrane level and through modulation of transcriptional regulation elements. These, along with other implicated pathways from the overall SNI-SARS-CoV-2 31dpi comparison, such as amyloid-beta binding and TRP channel modulation, are highlighted in **Figure 6D**.

Combined, this meta-analysis emphasizes SARS-CoV-2's ability to recapitulate transcriptional perturbations in the DRG underlying both inflammatory- and nerve injury-associated pain states. However, these findings also demonstrate the induction of plasticity-associated perturbations that counter those seen in other injury models. Future studies will elucidate whether these differences promote the maintenance of mechanical hypersensitivity we observed in SARS-CoV-2-infected animals. Furthermore, these findings support the use of the SARS-CoV-2 respiratory infection hamster model as a preclinical chronic pain model, which can be used for the understanding of the evaluation of pharmacological treatments.

DISCUSSION

The relatively high prevalence of both acute asymptomatic SARS-CoV-2 cases and positive somatosensory abnormalities in long COVID-19 patients prompted our group to investigate the ability of SARS-CoV-2 to perturb sensory nervous system functions. By utilizing the established golden hamster model of COVID-19 *(100, 101)*, we detected low levels of SARS-CoV-2-derived RNA in the absence of infectious particles. Exposure of sensory tissues to this viral material and/or the resulting type I interferon response correlated with a progressive and prolonged mechanical hypersensitivity signature that was unique to SARS-CoV-2. Transcriptomic analysis of thoracic SARS-CoV-2-infected DRGs highlighted a pronounced neuronal signature unlike the predominantly pro-inflammatory signature seen in IAV-infected DRGs. SARS-CoV-2 infection also correlated with worsened hypersensitivity post-recovery in

both female and male hamsters, which may be attributable to altered excitability, cytoskeletal architecture, extracellular remodeling, and myelination as a result of the host response to this inflammatory material. Transcriptional profiling of tDRGs at 1, 4, and 31dpi implicated several potential therapeutic targets for the management of chronic pain. Indeed, the prediction of ILF3 inhibition as a potential therapeutic intervention was validated in the murine CFA model of peripheral inflammation. Lastly, meta-analysis against existing transcriptional data sets from pain models highlighted several unexplored acutely and chronically contra-regulated genes between SARS-CoV-2 and SNI that could serve as future targets for anti-nociceptive therapies and provide novel mechanistic insight into these perturbations.

The SARS-CoV-2 RNA infiltration dynamics within sensory tissue observed in this study were similar to those noted in our longitudinal study of SARS-CoV-2 effects on the brain, where a rapid transcriptional induction to infection is followed by a return to baseline in most, but not all tissues *(32)*. While we confirmed the presence of SARS-CoV-2 RNA in various cell types of the DRG, we were surprised by the neuronally-biased transcriptional responses associated with this positivity that were not as prominent in tissue from IAV-infected hamsters. Together, these data suggest that the host response to SARS-CoV-2 infection elicits a unique transcriptional output capable of inducing lasting changes to DRG plasticity.

In addition to elucidating the impact SARS-CoV-2 has on DRGs, this study also identified a subset of host factors as modulators of the nociceptive responses. Of note, increased activity of ILF3 *(102–104)* is generally considered oncogenic. Furthermore, several of the disease risk signatures associated with gene changes observed in the 31dpi SARS-CoV-2 DRGs revolved around neuronal and glial cancers. Given our group and other's current (ILF3 inhibitor) and prior (*Rgs4* downregulation *(80)*, HDAC1 inhibition *(105)*, and HDAC6 *(106)* inhibition) successes with use of cancer-targeting therapies for the treatment of inflammatory- and nerve injury-associated pain states, we believe that the careful repurposing of existing

clinically-validated cancer therapeutics may serve as one possible strategy for providing alternative treatments for pain management. Implementation of this treatment strategy will necessitate molecular modifications or intricate drug delivery strategies to reduce potential systemic toxicities.

Future studies will focus on robust characterization of predicted pathways and validation of novel treatment interventions. For example, Ephrin Receptor Signaling, which frequently appeared in our ontology analyses, has a documented role in nociceptive processing *(107)*. Ephrin signaling is an essential mediator of extracellular matrix dynamics *(108)*, which subsequently affect synaptic plasticity in the form of neurite outgrowth and synaptic integrity *(109)*. Current pain therapeutics are primarily focused on modulating maladaptive neuronal hyperexcitability through GPCR or ion channel targeting *(110)*. However, few interventions target downstream transcriptomic mechanisms that broadly influence synaptic plasticity, an essential component of central sensitization. Along with ILF3, upstream regulators of the SARS-CoV-2-activated Ephrin pathway may support this alternative treatment direction.

Furthermore, few pain therapeutics target both the peripheral and central site of the nociceptive pathway. Here, we identified that several common predicted upstream regulator targets exist between the DRGs and brain regions that process pain and emotion. While most of the top common URs were counter-regulated between the DRGs and Thalamus/Striatum, three promising pain- and affect-associated URs (PTPRR, miR17HG, and FIRRE) were predicted to change unidirectionally between DRG and Thalamus. Work from our group has shown a high level of treatment effectiveness in targeting the same protein in DRG and Thalamus through studies on the signal transduction modulator RGS4 *(80 and unpublished)*. Notably, in this study, the expression of the *Rgs4* gene was decreased in 1dpi in DRGs of SARS-CoV-2-infected hamsters.

Finally, while several groups have recapitulated human COVID-19 symptoms in this respiratory hamster model, this is the first study that confirmed the model's relevance for somatosensory symptoms. From a mechanical hypersensitivity perspective, we believe this model accurately aligns with the somatosensory trajectory of many COVID-19 patients, both acutely and chronically. This SARS-CoV-2 model was also useful for further identifying core mechanisms across pain models, while also potentially providing insights into novel viral-mediated nociceptive states with relevance for drug development.

METHODS

Infection & Local Inflammation Animal Models

One- to two-month-old male golden hamsters (*Mesocricetus auratus*) were used in all infection experiments, and age-matched female hamsters were included in 31dpi experiments (Charles River Laboratories, MA). Male hamsters were co-housed on a twelve-hour light-dark cycle and had access to food and water *ad libitum*. Female hamsters were housed individually to prevent injury due to aggression. Hamster work was performed in a CDC/USDA-approved biosafety level 3 laboratory in accordance with NYU Langone and Icahn School of Medicine at Mount Sinai IACUC protocols. Mice were housed on a twelve-hour light-dark cycle and had access to food and water *ad libitum* in accordance with the Icahn School of Medicine at Mount Sinai IACUC protocols.

Two- to three-month-old hamsters received an intranasal inoculation of 100µL of phosphate-buffered saline (PBS) containing 1000 plaque forming units (PFU) of SARS-CoV-2, 100,000 PFU of IAV (viral control), or PBS alone (mock control). Hamsters were euthanized by intraperitoneal pentobarbital injection followed by cardiac perfusion with 60 mL PBS.

For studies using models of peripheral inflammation, two- to three-month old mice received 30uL left hindpaw injections of Complete Freund's Adjuvant (CFA; diluted 1:1 in

494 saline), as described *(106)*. For studies using the post-operative incision model, two- to three-
495 month old mice received an incision from the posterior plantar surface of the hindpaw to the
496 middle of the paw pads, in which dermis and superficial muscle was cut and dermis was sutured
497 afterwards as cited *(111)*. CFA and paw incision groups of mice received daily intraperitoneal
498 (i.p.) injections of saline (vehicle) or YM155 (Tocris Biosciences), an Interleukin Enhancer
499 Binding Factor 3 (ILF3) inhibitor (5mg/kg diluted in saline).

500 ***Von Frey Assay***

501 Hamsters/mice were placed on a raised grid platform in plastic containers and were
502 allowed to habituate to their environment for a minimum of 10 minutes. Afterwards, filaments of
503 ascending forces were applied to the left hindpaw and responses were recorded. A positive
504 response consisted of a hindpaw lift, shake, or lick. Progression to the next filament was
505 determined by recording of positive or negative responses for three out of five applications with
506 each filament. Mechanical withdrawal threshold was defined as the first (for hamsters, to
507 minimize cross-contamination of cohorts by prolonged fomite exposure) or second (mouse, for
508 consistency) filament force at which an animal had three positive responses. All materials
509 utilized for testing of infected hamsters were thoroughly decontaminated between testing of
510 infection groups.

511 ***Hargreave's Assay***

512 The CFA model induces thermal hypersensitivity for 10-14 days on average *(80)*. We
513 used the Hargreave's thermal beam assay to assess the effects of YM155 administration on
514 thermal hypersensitivity associated with left hindpaw CFA injection. Mice were placed on a
515 Hargreave's platform in plastic containers and were allowed to habituate for 30 minutes. A light
516 beam heat source (IITC Life Science Inc., CA) set to an intensity level of IF=30 was aimed at
517 the left hindpaw for a maximum of 20 seconds (cutoff). Similarly to Von Frey, paw withdrawal

518 was defined as a hindpaw lift, shake, or lick. Three measurements were recorded and averaged
519 for each hindpaw, with each measurement taking place at least two minutes apart.

520 ***Tissues***

521 Tissues were harvested at 1, 4, and 31 dpi and immediately placed in TRIzol (Invitrogen,
522 MA) for transcriptomic analysis or 4% paraformaldehyde (PFA) in phosphate-buffered saline
523 (PBS) for histology or fluorescent *in situ hybridization* (RNAscope). Fixed tissues were sucrose
524 converted after 48 hours of 4% PFA fixation in 10% sucrose in PBS (Day 1), 20% sucrose in
525 PBS (Day 2), and 30% sucrose in PBS with 0.01% azide (Day 3). Slide-mounted tissues were
526 paraffin-embedded and sliced to a thickness of 5 microns. Tissue collected for transcriptomic
527 analysis were homogenized in Lysing Matrix A homogenization tubs (MP Biomedicals, CA) for
528 two cycles (40s; 6m/s) in a FastPrep 24 5g bead grinder and lysis system (MP Biomedicals,
529 CA). Tissue collected for plaque assays was homogenized in 1 mL PBS in Lysing Matrix A
530 homogenization tubs (MP Biomedicals, CA) for two cycles (40s; 6m/s).

531 ***RNA Isolation & qPCR***

532 RNA was isolated through a phenol:chloroform phase separation protocol as detailed in
533 the TRIzol Reagent User Guide. RNA concentrations were measured by NanoDrop
534 (Thermofisher, MA). 1,000ng of cDNA was synthesized using the qScript cDNA Synthesis kit
535 (QuantaBio, MA) as detailed in the qScript cDNA Synthesis Kit Manual. Exon-exon-spanning
536 primers targeting as many splice variants as possible were designed with Primer-BLAST
537 (National Center for Biotechnology Information, MD). qPCRs were performed in triplicate with 30
538 ng of cDNA and a master mix of exon-spanning primers (Supplementary Table 1) and PerfeCTa
539 SYBR Green FastMix ROX (QuantaBio, MA) on an QuantStudio real-time PCR analyzer
540 (Invitrogen, MA), and results were expressed as fold change ($2^{-\Delta\Delta Ct}$) relative to the β-actin gene
541 (*Actb*).

Plaque Formation Assay

Plaque assays were performed as described previously *(31)*. Virus was logarithmically diluted in SARS-CoV-2 infection medium with a final volume of 200 uL volume per dilution. 12-well plates of Vero E6 cells were incubated for 1 hour at room temperature with gentle agitation every 10 minutes. An overlay comprised of Modified Eagle Medium (GIBCO), 4 mM L-glutamine (GIBCO), 0.2% BSA (MP Biomedicals), 10 mM HEPES (Fisher Scientific), 0.12% $NaHCO_3$, and 0.7% Oxoid agar (Thermo Scientific) was pipetted into each well. Plates were incubated at 37 degrees C for 48 hours prior to fixation in 4% PFA in PBS for 24 hours. Plaques were visualized via staining with crystal violet solution (1% crystal violet (w/v) in 20% ethanol (v/v)) for 15 minutes.

RNAscope In Situ Hybridization

The Fluorescent Multiplex V2 kit (Advanced Cell Diagnostics, CA) was used for RNAscope FISH. Specifically, we used the FFPE protocol as detailed in the RNAscope Multiplex Fluorescent Reagent Kit v2 Assay User Manual. RNAscope probes were as follows: *Rbfox3* (NeuN) for pan-neuronal labeling (Mau-Rbfox3-C1) and the Spike gene (*S*) for SARS-CoV-2 labeling (V-nCoV2019-S-C3). Opal dyes (Akoya Biosciences, MA) were used for secondary staining as follows: Opal 690 for C1 and Opal 570 for C3. DAPI was used for nuclear staining. Images were taken on an LSM880 confocal microscope (Zeiss, GER) with identical parameters between mock and SARS samples.

Immunohistochemistry

Immunohistochemistry was performed according to protocols described previously *(32)*. Briefly, 5µm sections were cut from FFPE tissues and mounted on charged glass slides. Sections were deparaffinized by immersion in xylene and subsequently submerged in decreasing concentrations of ethanol to rehydrate. Rehydrated sections were submerged in

IHC-Tek Epitope Retrieval Solution (Cat #IW-1100) and steamed for 45min in IHC-Tek Epitope Retrieval Steamer (Cat #IW-1102) for antigen retrieval. Tissues were blocked with 10% goat serum and 1% bovine serum albumin in TBS for 1hr at room temperature. Primary antibody (monoclonal murine-derived anti-SARS-CoV-2 N protein) was diluted 1:100 in a 1% BSA TBS solution and added to slides. Slides were incubated with primary antibody solution overnight at 4°C. Slides were washed in TBS with 0.025% Triton-X-100 and treated with 0.3% hydrogen peroxide in TBS for 15min. Slides were washed once again. HRP-conjugated goat anti-mouse IgG secondary antibody (ThermoFisher, Cat #A21426) was diluted 1:5000 and added to slides. Slides incubated with secondary antibody at room temperature for 1hr. Slides were washed twice, and DAB developing reagent (Vector Laboratories, Cat #SK-4105) was added to slides. Slides were dehydrated with increasing concentrations of ethanol and cleared using xylene. Slides were cover slipped, dried, and imaged using brightfield setting on EVOS M5000 inverted microscope.

RNA Sequencing

RNA was isolated from tissues as previously described above. 500ng-1µg of total RNA per sample was enriched for polyadenylated RNA and prepared for RNA sequencing using the TruSeq Stranded mRNA Library Prep Kit (Illumina) per manufacturer instructions. Samples were sequenced on an Illumina NextSeq 500 platform or by the NYU Langone Genome Technology Center. FASTQ files were then aligned to the golden hamster genome (MesAur 1.0, ensembl) via the RNA-Seq Alignment application (BaseSpace, Illumina). Salmon files were analyzed using DESeq2 *(112)*. For non-ontology analyses, all genes with an adjusted p-value (p-adj) less than 0.1 were considered “Differentially Expressed Genes” (DEGs).

Ontological analysis was performed using g:Profiler and Qiagen Ingenuity Pathway Analysis, targeting genes with a nominal p-value of less than 0.05 to increase analytical power. All visualizations of RNA-seq, differential expression analysis, and ontological analysis data

were created by the respective ontological analysis programs or by R using ggplot2, VennDiagram, Circos, pheatmap, ComplexHeatmap, and gplots packages.

Gene set enrichment analyses were conducted using the GSEA Java application for Mac (v 4.1.0) (MSigDB; Broad Institute, UC San Diego). Analyses were performed on pre-ranked gene lists derived from differential expression data. Genes were ranked by the following statistic: -log10(p-value)/sign(log2FoldChange). GSEA analyses were conducted against the C8 cell type signature gene set (v7.4) provided by the Molecular Signatures Database (MSigDB).

Meta-Analysis

FASTQ files from Parisien et al. (2019) *(99)* generated from RNA-seq of DRG tissues from mice subjected to sham (mock), Complete Freund's Adjuvant (CFA), and Spared Nerve Injury (SNI) treatments were obtained from NCBI GEO (GSE111216). Paired end read files were aligned to the *Mus musculus* transcriptome (GRCm39) and quantified using Salmon (version 1.4.0). Salmon files were analyzed for differentially expressed genes using DESeq2, and all genes expressing a p-adj<0.1 were considered differentially expressed. Differentially expressed genes from murine DRG injury models compared to mock tissues were compared to analogous differentially expressed genes from infected hamster DRG tissues compared to mock hamster DRG tissues. These comparative analyses were visualized using Circos, VennDiagram, and ggplot2. Shared and contra-regulated gene sets highlighted from these analyses were also analyzed for ontology using g:Profiler.

Statistical Analyses

All statistical analyses outside of sequencing-related assays were performed in GraphPad Prism Version 10. Repeated measure one- and two-way ANOVAs were used to compare the effects of virus type and time of infection on mechanical hypersensitivity, and post-

hoc Tukey's multiple comparison test were used to perform timepoint comparisons for the Von Frey assay. Multiple t-tests and two-way ANOVAs were used for qPCR analysis.

RNA-seq data was analyzed as described above. Ontology analysis statistics were performed with either Ingenuity Pathway Analysis (IPA), g:Profiler, or Enrichr *(113)*.

FIGURE LEGENDS

Figure 1. **Viral mRNA and interferon-stimulated transcripts are acutely elevated in dorsal root ganglia & spinal cord by qPCR. A-B, E-F)** Nucleocapsid protein-encoding gene (*N*) was significantly elevated in the cervical and thoracic segments of DRGs and SC at 1dpi, but not 4, 7, or 14dpi of SARS-CoV-2-infected hamsters (n=3-8/group). **C-D, G-H)** Interferon-stimulated gene 15 (*Isg15*) was significantly elevated at 1 and 4dpi at both DRG and SC levels in SARS-CoV-2-infected animals (n=3-8 per group). **I)** Plaque formation assay demonstrates mature virus presence only in the lungs of SARS-CoV-2-infected hamsters at 3dpi, but not DRG or SC (n=4 per group). $\Phi p<0.05$ for two-way ANOVA interaction factor; $*p<0.05$, $**p<0.01$ for multiple t-tests.

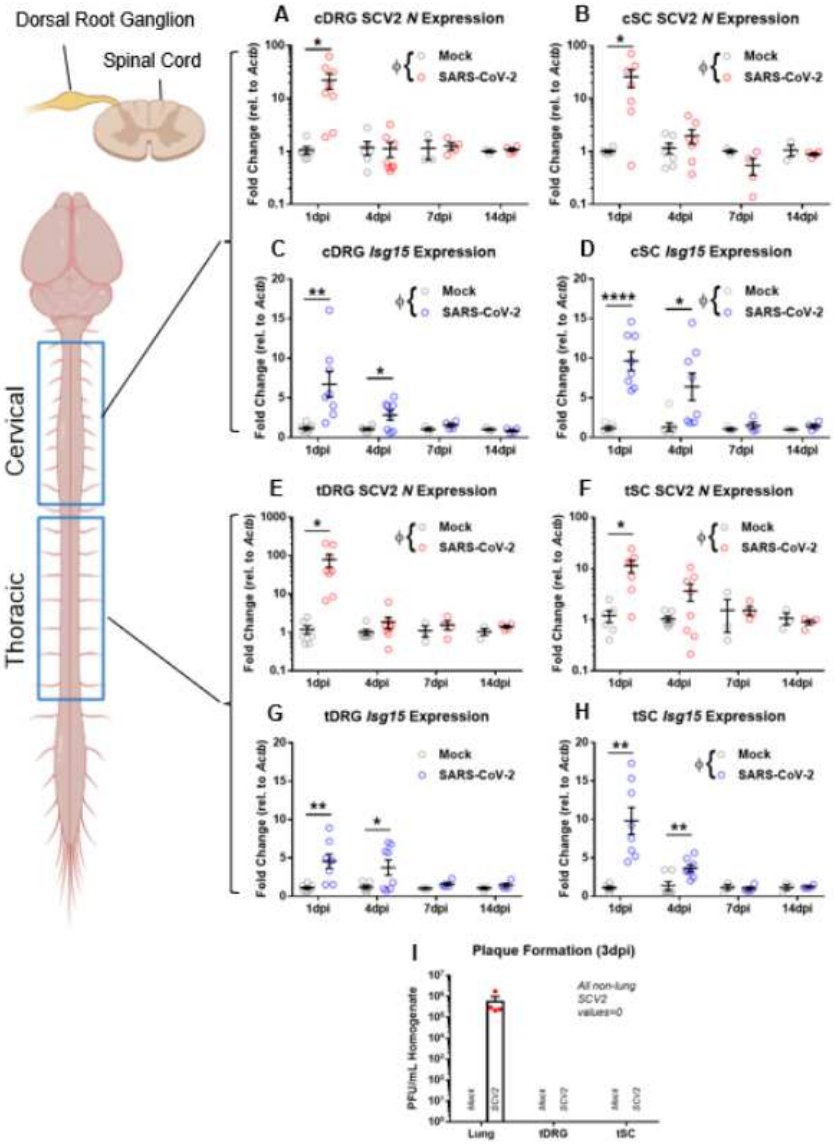

628

629 ***Figure 2.*** **Viral mRNA is visibly detectable in DRG and SC by ISH, but mature virus is not**
630 **detectable by IHC. A)** Spike RNA (red) is detectable around DAPI (blue) and Rbox3 (white) in
631 cervical and thoracic DRGs of SARS-CoV-2-infected animals but not mocks, suggesting
632 infiltration of glial and neuronal cells at 1dpi (n=2/group). **B)** Spike RNA (red) is detectable
633 around DAPI (blue) in cervical and thoracic SC, but not in mock SC at 1dpi (n=2 per group). **C)**
634 Nucleocapsid protein was not detectable in cervical or thoracic DRGs of SARS-CoV-2-infected
635 or mock animals, but it was detectable in lung tissue of SARS-CoV-2-infected animals at 1dpi
636 (n=2 per group).

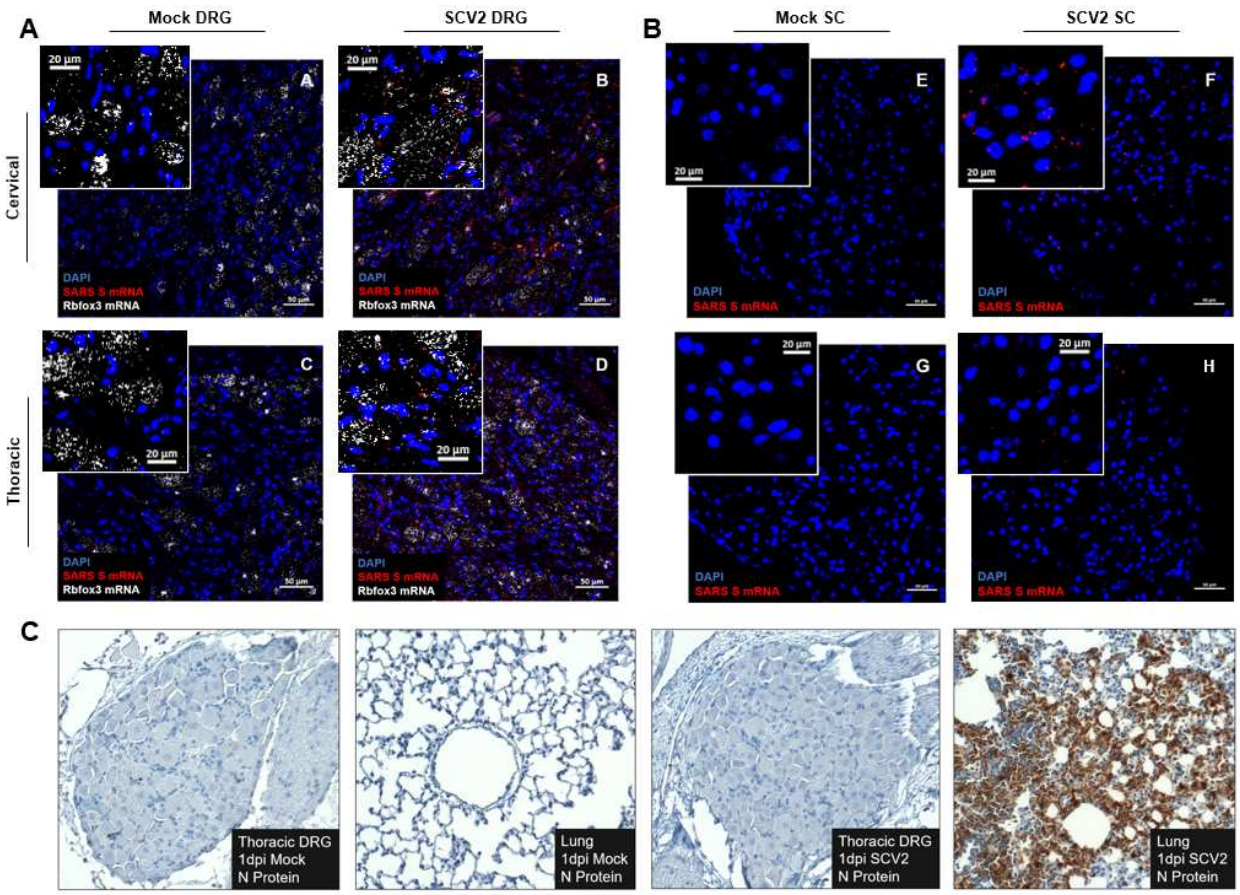

Figure 3. **SARS-CoV-2 induces a unique behavioral phenotype and molecular signature in DRG tissue. A)** Mechanical thresholds of mock, IAV, and SARS-CoV-2 animals at baseline, 1dpi, and 4dpi. IAV induced severe hypersensitivity at 1dpi, and SARS-CoV-2 induced mild hypersensitivity by 4dpi (n=4 per group; *p<0.05 for one-way ANOVA Tukey's m.c.). IAV infection resulted in significantly lower thresholds than SARS-CoV-2 on 1dpi (Φp<0.05 for two-way ANOVA Tukey's m.c.). **B)** Volcano plots for 1 and 4dpi SARS-CoV-2 and IAV tDRG RNA-seq (n=4 per group). Red=p-adj.<0.1, log2FC>0. Blue=p-adj.<0.1, log2FC>0. Green=p-nom.<0.05. **C)** Top 5 IPA Canonical Pathways for SARS-CoV-2 and IAV tDRGs (p-nom.<0.05; -$\log_{10}$(p-value)>1.3). **D)** Petal diagrams for 1dpi and 4dpi SARS-CoV-2 and IAV tDRG DEGs (p-adj.<0.01), with commonly upregulated or downregulated genes. **E)** qPCR validation of 1dpi and 4dpi SARS-CoV-2 tDRG DEGs (n=3-8 per group; *p<0.05, ****p<0.0001 for multiple t-tests). **F)** IPA predicted upstream regulators that had predicted inhibition in 1 and 4dpi SARS-CoV-2

650 tissues and 4dpi IAV tissues (*Benjamini-Hochberg p<0.05). **G)** No significant changes in *Ilf3*
651 gene expression were observed in SARS-CoV-2, IAV, or Mock tDRGs 1 and 4dpi in accordance
652 with sequencing (n=4-8 per group). **H)** IPA prediction of ILF3-regulated genes at 1 and 4dpi in
653 SARS-CoV-2 tDRGs.

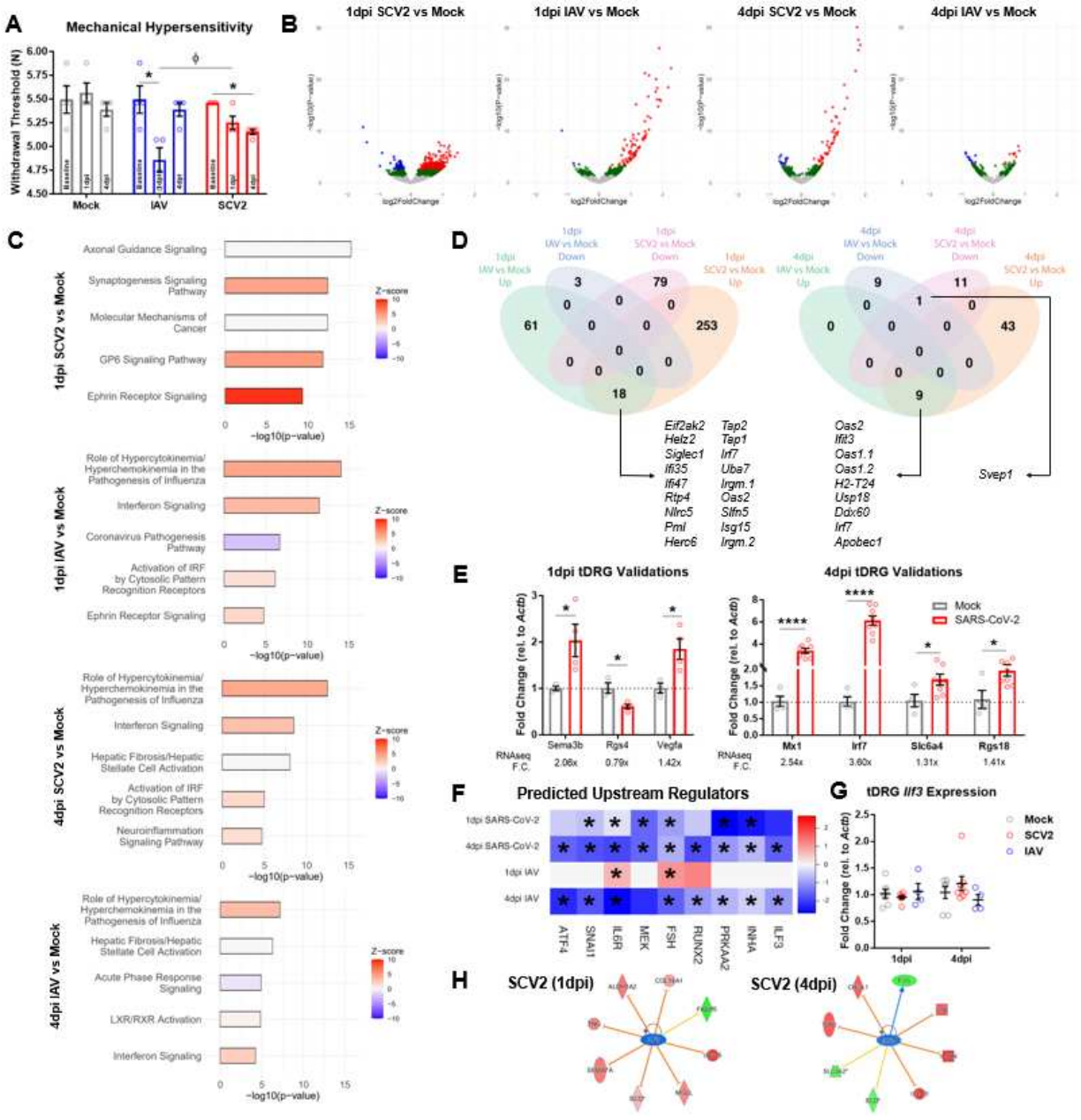

654

655 ***Figure 4.*** **YM155 alleviates CFA-induced thermal and mechanical hypersensitivity in an**
656 **immediate and sustained fashion. A-B)** YM155 (5mg/kg i.p. QD) increased thermal and

mechanical thresholds 30-60 minutes after administration (*p<0.05, ****p<0.0001 for two-way ANOVA Sidak's m.c.) (n=6 per group). **C-D)** YM155 increased thermal and mechanical thresholds in a sustained fashion ~24 hours after administration by 5-6 days after initial administration (*p<0.05, **p<0.01, ***p<0.001 for two-way ANOVA Sidak's m.c.) (n=6 per group). **E)** No changes in post-CFA weight were observed in YM155 animals throughout the course of administration (n=6 per group). **F)** Pre-treatment with YM155 led to significantly lower mechanical hypersensitivity after paw incision (*p<0.05 for two-way ANOVA Sidak's m.c.) (n=6 per group). **G)** No differences in locomotion were observed on Day 1 post-paw incision between YM155 and Saline mice (n=6 per group).

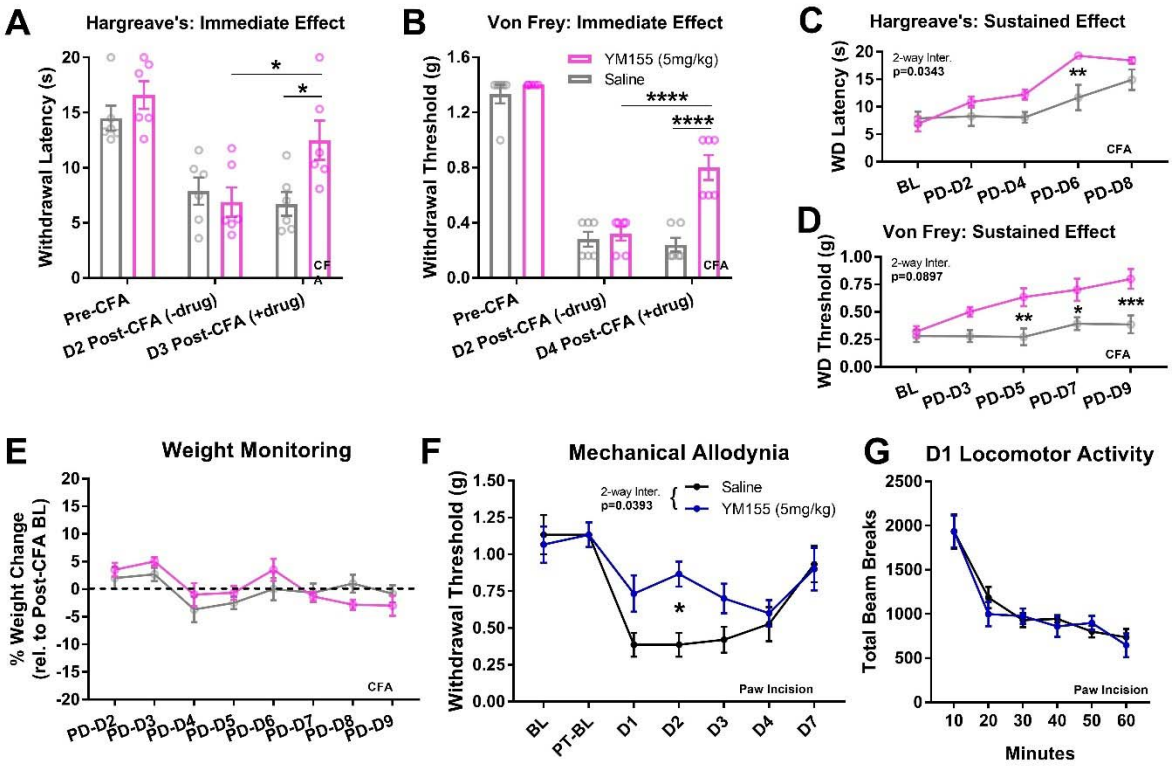

Figure 5. **SARS-CoV-2 infection results in substantially reduced mechanical thresholds and a neuropathic transcriptomic landscape in the tDRGs well after viral clearance. A)** Mechanical thresholds of mock, IAV, and SARS-CoV-2 animals at 28dpi (n=6 per group;

670 **p<0.01, ****p<0.0001 for one-way ANOVA Tukey's m.c.). **B)** Volcano plot for 31dpi SARS-
671 CoV-2 tDRG RNA-seq (n=3 per group). Red=p-adj.<0.1, log2FC>0. Blue=p-adj.<0.1, log2FC>0.
672 Green=p-nom.<0.05. **C)** IPA top 10 canonical pathways (-log10(p-value)>1.3) associated with
673 31dpi SARS-CoV-2 tDRG DEGs (p-nom.<0.05). **D)** enrichr DisGENET gateway top 10 diseases
674 associated with 31 dpi SARS-CoV-2 tDRG DEGs (p-nom.<0.05). **E)** Log_2(FC) of select neuronal
675 and inflammatory genes from 31dpi RNA-seq (p-adj.<0.1). **F)** Positively and negatively
676 enriched cell subtypes associated with 31dpi SARS-CoV-2 tDRG DEGs (GSEA NES>|1.5|;
677 DEG p-adj.<0.1)**. G)** IPA top 15 upstream regulators between 31dpi SARS-CoV-2 tDRG,
678 Striatum, and Thalamus (DEG p-nom.<0.05).

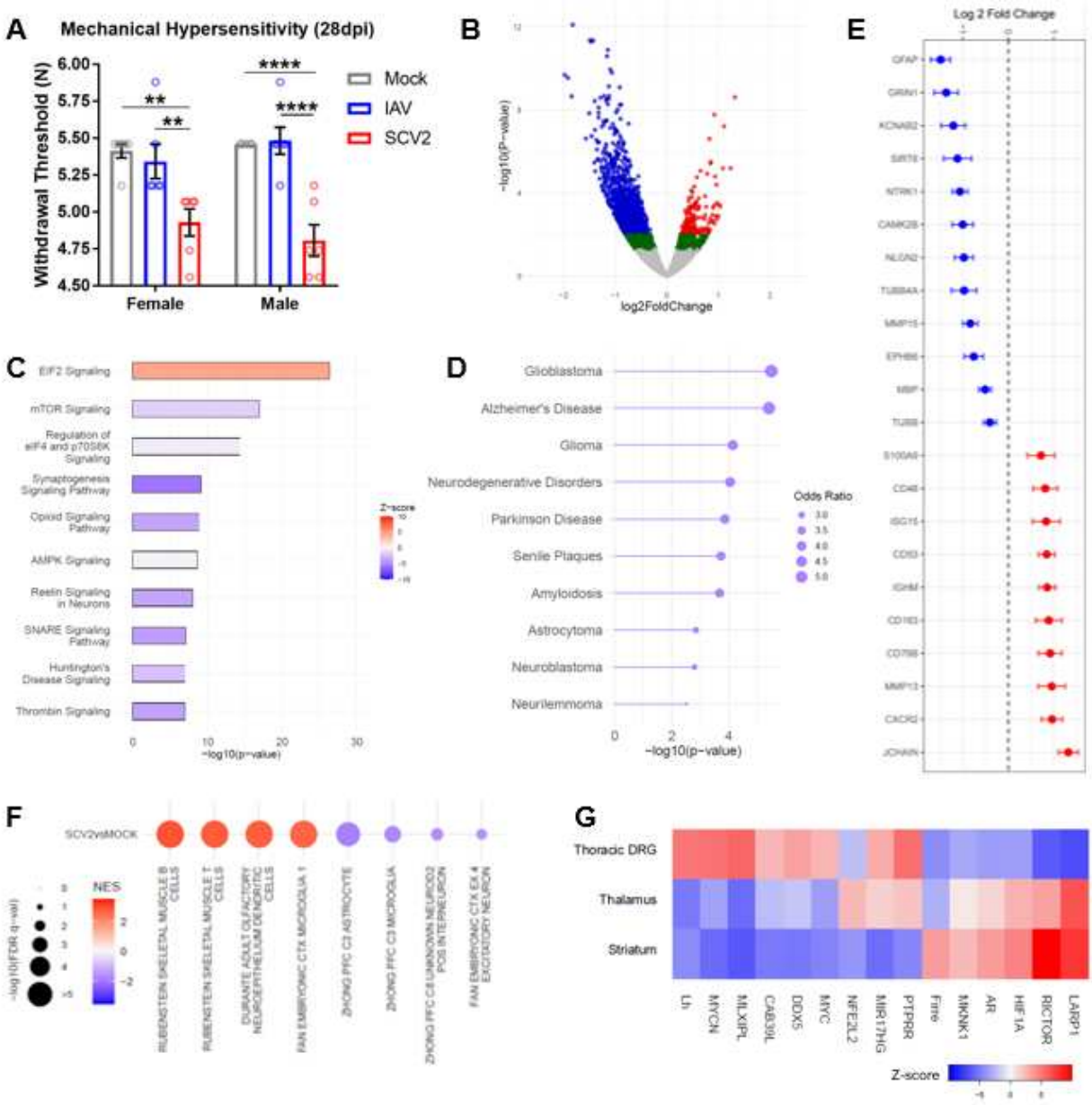

679

680 ***Figure 6.*** **SARS-CoV-2 infection causes a longitudinally variable tDRG transcriptomic**
681 **profile that shares pro-nociceptive components yet demonstrates unique plasticity**
682 **signatures. A)** Chord diagrams demonstrating regulation of DRG gene expression changes
683 between CFA, SNI, and SARS-CoV-2 (1, 4, and 31dpi) animals. **B-D)** Dot plots demonstrating
684 significant Gene Ontology (GO; Molecular Function, Biological Process, Cellular Compartment),
685 Kyoto Encyclopedia of Genes and Genomces (KEGG), Reactome (REAC), WikiPathways (WP),

Transfac (TF), and Human Protein Atlas (HPA) (-log10p-adj.>1.3) for contra-regulated genes between SNI and 1dpi SARS-CoV-2, conserved upregulated genes for CFA/SNI vs 1-4dpi SARS-CoV-2 comparisons, and all commonly regulated genes between SNI & 31dpi SARS-CoV-2. Dot plots adapted from g:Profiler.

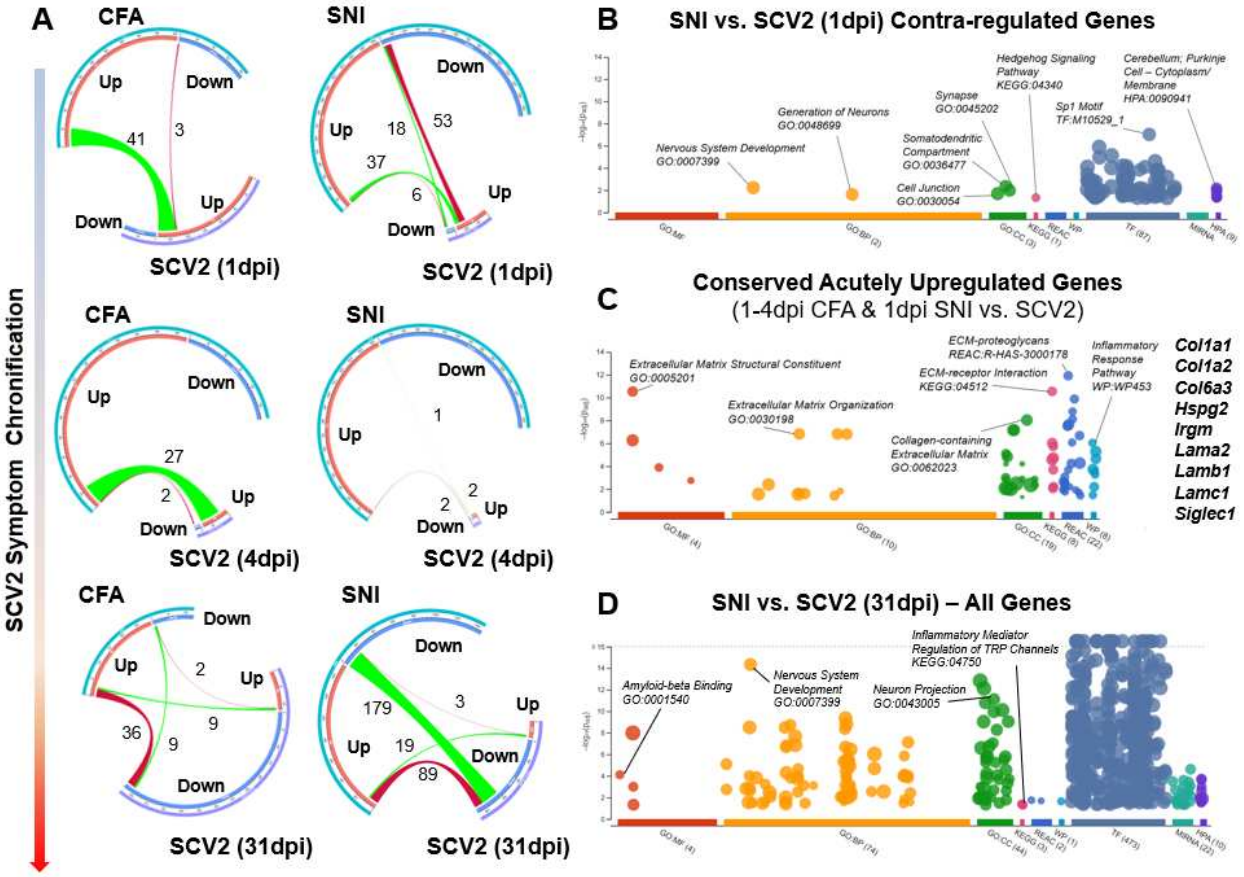

ACKNOWLEDGEMENTS

We would like to further thank Francis Avila, Virginia Gillespie, DVM, Ying Dai, and the rest of the staff at the Mount Sinai Center for Comparative Medicine and Surgery and the Mount Sinai Biorepository and Pathology Core for their technical assistance in tissue preparation for histology.

FUNDING

This study was supported by National Institute of Neurological Disorders and Stroke NS086444S1 (R.A.S), the Zegar Family Foundation (B.T.) and the Friedman Brain Institute Research Scholars Program (V.Z., B.T., R.A.S., J.J.F.).

AUTHOR CONTRIBUTIONS

Study concept and design: RAS, JJF, BT, VZ. Tissue Harvesting: RAS, JJF, KDP. Quantitative PCR and Plaque Assays: RAS, JJF, I. Golynker. RNAscope & IHC: JZ & JJF. RNA-seq & Data Analysis: RAS, JJF. Behavioral Assays: RAS, JJF, I. Giosan. Supervision: BT, VZ. Drafting of original manuscript: RAS, JJF. All authors reviewed, revised, and approved the final version of this paper.

COMPETING INTERESTS

The authors have no competing interests to disclose.

DATA AND MATERIALS AVAILABILITY

RNAseq data will be uploaded to NCBI GEO upon prior to publication of the manuscript for public accessibility. Other data may be provided upon request.

References

1. G. Pascarella, A. Strumia, C. Piliego, F. Bruno, R. Del Buono, F. Costa, S. Scarlata, F. E. Agrò, COVID-19 diagnosis and management: a comprehensive review*J. Intern. Med.* **288** (2020), doi:10.1111/joim.13091.

2. E. Caronna, A. Ballvé, A. Llauradó, V. J. Gallardo, D. María Ariton, S. Lallana, S. L. Maza, M. O. Gadea, L. Quibus, J. L. Restrepo, M. Rodrigo-Gisbert, A. Vilaseca, M. H. Gonzalez, M. M. Gallo, A. Alpuente, M. Torres-Ferrus, R. P. Borrell, J. Alvarez-Sabin, P. Pozo-Rosich, Headache: A striking prodromal and persistent symptom, predictive of COVID-19 clinical evolution. *Cephalalgia* **40** (2020), doi:10.1177/0333102420965157.

3. M. Amanat, N. Rezaei, M. Roozbeh, M. Shojaei, A. Tafakhori, A. Zoghi, I. A. Darazam, M. Salehi, E. Karimialavijeh, B. S. Lima, A. Garakani, A. Vaccaro, M. Ramezani, Neurological manifestations as the predictors of severity and mortality in hospitalized individuals with COVID-19: a multicenter prospective clinical study. *BMC Neurol.* **21** (2021), doi:10.1186/s12883-021-02152-5.

4. S. Escalard, V. Chalumeau, C. Escalard, H. Redjem, F. Delvoye, S. Hébert, S. Smajda, G. Ciccio, J. P. Desilles, M. Mazighi, R. Blanc, B. Maïer, M. Piotin, Early brain imaging shows

increased severity of acute ischemic strokes with large vessel occlusion in COVID-19 patients. *Stroke* (2020), doi:10.1161/STROKEAHA.120.031011.

5. M. K. Halushka, R. S. Vander Heide, Myocarditis is rare in COVID-19 autopsies: cardiovascular findings across 277 postmortem examinations. *Cardiovasc. Pathol.* **50** (2021), doi:10.1016/j.carpath.2020.107300.

6. J. S. Stevens, K. L. King, S. Y. Robbins-Juarez, P. Khairallah, K. Toma, H. A. Verduzco, E. Daniel, D. Douglas, A. A. Moses, Y. Peleg, P. Starakiewicz, M. T. Li, D. W. Kim, K. Yu, L. Qian, V. H. Shah, M. R. O'Donnell, M. J. Cummings, J. Zucker, K. Natarajan, A. Perotte, D. Tsapepas, K. Krzysztof, G. Dube, E. Siddall, S. Shirazian, T. L. Nickolas, M. K. Rao, J. M. Barasch, A. M. Valeri, J. Radhakrishnan, A. G. Gharavi, S. A. Husain, S. Mohan, High rate of renal recovery in survivors of COVID-19 associated acute renal failure requiring renal replacement therapy. *PLoS One* **15** (2020), doi:10.1371/journal.pone.0244131.

7. X. J. Song, D. L. Xiong, Z. Y. Wang, D. Yang, L. Zhou, R. C. Li, Pain Management during the COVID-19 Pandemic in China: Lessons Learned*Pain Med. (United States)* (2020), doi:10.1093/PM/PNAA143.

8. M. A. Ellul, L. Benjamin, B. Singh, S. Lant, B. D. Michael, A. Easton, R. Kneen, S. Defres, J. Sejvar, T. Solomon, Neurological associations of COVID-19*Lancet Neurol.* (2020), doi:10.1016/S1474-4422(20)30221-0.

9. S. Andalib, J. Biller, M. Di Napoli, N. Moghimi, L. D. McCullough, C. A. Rubinos, C. O'Hana Nobleza, M. R. Azarpazhooh, L. Catanese, I. Elicer, M. Jafari, F. Liberati, C. Camejo, M. Torbey, A. A. Divani, Peripheral Nervous System Manifestations Associated with COVID-19*Curr. Neurol. Neurosci. Rep.* (2021), doi:10.1007/s11910-021-01102-5.

10. A. Carfì, R. Bernabei, F. Landi, Persistent symptoms in patients after acute COVID-19*JAMA - J. Am. Med. Assoc.* **324** (2020), doi:10.1001/jama.2020.12603.

11. K. Stavem, W. Ghanima, M. K. Olsen, H. M. Gilboe, G. Einvik, Persistent symptoms 1.5-6 months after COVID-19 in non-hospitalised subjects: A population-based cohort study. *Thorax* **76** (2021), doi:10.1136/thoraxjnl-2020-216377.

12. A clinical case definition of post COVID-19 condition by a Delphi consensus, 6 October 2021. *World Heal. Organ.* (2021).

13. C. H. Sudre, B. Murray, T. Varsavsky, M. S. Graham, R. S. Penfold, R. C. Bowyer, J. C. Pujol, K. Klaser, M. Antonelli, L. S. Canas, E. Molteni, M. Modat, M. Jorge Cardoso, A. May, S. Ganesh, R. Davies, L. H. Nguyen, D. A. Drew, C. M. Astley, A. D. Joshi, J. Merino, N. Tsereteli, T. Fall, M. F. Gomez, E. L. Duncan, C. Menni, F. M. K. Williams, P. W. Franks, A. T. Chan, J. Wolf, S. Ourselin, T. Spector, C. J. Steves, Attributes and predictors of long COVID. *Nat. Med.* (2021), doi:10.1038/s41591-021-01292-y.

14. H. E. Davis, G. S. Assaf, L. McCorkell, H. Wei, R. J. Low, Y. Re'em, S. Redfield, J. P. Austin, A. Akrami, Characterizing long COVID in an international cohort: 7 months of symptoms and their impact. *EClinicalMedicine* (2021), doi:10.1016/j.eclinm.2021.101019.

15. L. Sigfrid, T. M. Drake, E. Pauley, E. C. Jesudason, P. Olliaro, W. S. Lim, A. Gillesen, C. Berry, D. J. Lowe, J. McPeake, N. Lone, D. Munblit, A. Casey, P. Bannister, C. D. Russell, L. Goodwin, A. Ho, L. Turtle, M. E. O'Hara, C. Hastie, C. Donohue, R. G. Spencer, C. Donegan, A. Gummery, J. Harrison, H. E. Hardwick, C. E. Hastie, G. Carson, L. Merson, J. K. Baillie, P. Openshaw, E. M. Harrison, A. B. Docherty, M. G. Semple, J. T. Scott, Long Covid in adults discharged from UK hospitals after Covid-19: A prospective, multicentre cohort study using the

772 ISARIC WHO Clinical Characterisation Protocol. *Lancet Reg. Heal. - Eur.* (2021),
773 doi:10.1016/j.lanepe.2021.100186.

774 16. H. J. Zhao, X. X. Lu, Y. Bin Deng, Y. J. Tang, J. C. Lu, COVID-19: Asymptomatic carrier
775 transmission is an underestimated problem. *Epidemiol. Infect.* (2020),
776 doi:10.1017/S0950268820001235.

777 17. Z. Gao, Y. Xu, C. Sun, X. Wang, Y. Guo, S. Qiu, K. Ma, A systematic review of
778 asymptomatic infections with COVID-19*J. Microbiol. Immunol. Infect.* (2021),
779 doi:10.1016/j.jmii.2020.05.001.

780 18. M. C. Rowbotham, K. L. Petersen, Zoster-associated pain and neural dysfunction*Pain*
781 (2001), doi:10.1016/S0304-3959(01)00328-1.

782 19. S. Verma, L. Estanislao, D. Simpson, HIV-associated neuropathic pain: Epidemiology,
783 pathophysiology and management. *CNS Drugs* **19**, 325–334 (2005).

784 20. Y. Wu, X. Xu, Z. Chen, J. Duan, K. Hashimoto, L. Yang, C. Liu, C. Yang, Nervous system
785 involvement after infection with COVID-19 and other coronaviruses*Brain. Behav. Immun.*
786 (2020), doi:10.1016/j.bbi.2020.03.031.

787 21. E. M. Garry, A. Delaney, H. A. Anderson, E. C. Sirinathsinghji, R. H. Clapp, W. J. Martin, P.
788 R. Kinchington, D. L. Krah, C. Abbadie, S. M. Fleetwood-Walker, Varicella zoster virus induces
789 neuropathic changes in rat dorsal root ganglia and behavioral reflex sensitisation that is
790 attenuated by gabapentin or sodium channel blocking drugs. *Pain* (2005),
791 doi:10.1016/j.pain.2005.08.003.

792 22. I. Takasaki, T. Andoh, K. Shiraki, Y. Kuraishi, Allodynia and hyperalgesia induced by herpes
793 simplex virus type-1 infection in mice. *Pain* (2000), doi:10.1016/S0304-3959(00)00240-2.

794 23. C. A. Pardo, J. C. McArthur, J. W. Griffin, in *Journal of the Peripheral Nervous System*,
795 (2001).

796 24. K. Maratou, V. C. J. Wallace, F. S. Hasnie, K. Okuse, R. Hosseini, N. Jina, J. Blackbeard, T.
797 Pheby, C. Orengo, A. H. Dickenson, S. B. McMahon, A. S. C. Rice, Comparison of dorsal root
798 ganglion gene expression in rat models of traumatic and HIV-associated neuropathic pain. *Eur.*
799 *J. Pain* (2009), doi:10.1016/j.ejpain.2008.05.011.

800 25. A. L. Oaklander, Clinical significance of angiotensin-converting enzyme 2 receptors for
801 severe acute respiratory syndrome coronavirus 2 (COVID-19) on peripheral small-fiber sensory
802 neurons is unknown today*Pain* (2020), doi:10.1097/j.pain.0000000000002050.

803 26. A. Paniz-Mondolfi, C. Bryce, Z. Grimes, R. E. Gordon, J. Reidy, J. Lednicky, E. M. Sordillo,
804 M. Fowkes, Central nervous system involvement by severe acute respiratory syndrome
805 coronavirus-2 (SARS-CoV-2)*J. Med. Virol.* (2020), doi:10.1002/jmv.25915.

806 27. J. Matschke, M. Lütgehetmann, C. Hagel, J. P. Sperhake, A. S. Schröder, C. Edler, H.
807 Mushumba, A. Fitzek, L. Allweiss, M. Dandri, M. Dottermusch, A. Heinemann, S. Pfefferle, M.
808 Schwabenland, D. Sumner Magruder, S. Bonn, M. Prinz, C. Gerloff, K. Püschel, S. Krasemann,
809 M. Aepfelbacher, M. Glatzel, Neuropathology of patients with COVID-19 in Germany: a post-
810 mortem case series. *Lancet Neurol.* **19** (2020), doi:10.1016/S1474-4422(20)30308-2.

811 28. B. Schurink, E. Roos, T. Radonic, E. Barbe, C. S. C. Bouman, H. H. de Boer, G. J. de Bree,
812 E. B. Bulle, E. M. Aronica, S. Florquin, J. Fronczek, L. M. A. Heunks, M. D. de Jong, L. Guo, R.
813 du Long, R. Lutter, P. C. G. Molenaar, E. A. Neefjes-Borst, H. W. M. Niessen, C. J. M. van
814 Noesel, J. J. T. H. Roelofs, E. J. Snijder, E. C. Soer, J. Verheij, A. P. J. Vlaar, W. Vos, N. N. van

der Wel, A. C. van der Wal, P. van der Valk, M. Bugiani, Viral presence and immunopathology in patients with lethal COVID-19: a prospective autopsy cohort study. *The Lancet Microbe* **1** (2020), doi:10.1016/S2666-5247(20)30144-0.

29. K. T. Thakur, E. H. Miller, M. D. Glendinning, O. Al-Dalahmah, M. A. Banu, A. K. Boehme, A. L. Boubour, S. S. Bruce, A. M. Chong, J. Claassen, P. L. Faust, G. Hargus, R. A. Hickman, S. Jambawalikar, A. G. Khandji, C. Y. Kim, R. S. Klein, A. Lignelli-Dipple, C. C. Lin, Y. Liu, M. L. Miller, G. Moonis, A. S. Nordvig, J. B. Overdevest, M. L. Prust, S. Przedborski, W. H. Roth, A. Soung, K. Tanji, A. F. Teich, D. Agalliu, A. C. Uhlemann, J. E. Goldman, P. Canoll, COVID-19 neuropathology at Columbia University Irving Medical Center/New York Presbyterian Hospital. *Brain* **144** (2021), doi:10.1093/brain/awab148.

30. T. Menter, J. D. Haslbauer, R. Nienhold, S. Savic, H. Hopfer, N. Deigendesch, S. Frank, D. Turek, N. Willi, H. Pargger, S. Bassetti, J. D. Leuppi, G. Cathomas, M. Tolnay, K. D. Mertz, A. Tzankov, Postmortem examination of COVID-19 patients reveals diffuse alveolar damage with severe capillary congestion and variegated findings in lungs and other organs suggesting vascular dysfunction. *Histopathology* **77** (2020), doi:10.1111/his.14134.

31. D. A. Hoagland, R. Møller, S. A. Uhl, K. Oishi, J. Frere, I. Golynker, S. Horiuchi, M. Panis, D. Blanco-Melo, D. Sachs, K. Arkun, J. K. Lim, B. R. tenOever, Leveraging the antiviral type I interferon system as a first line of defense against SARS-CoV-2 pathogenicity. *Immunity* **54** (2021), doi:10.1016/j.immuni.2021.01.017.

32. J. J. Frere, R. A. Serafini, K. D. Pryce, M. Zazhytska, K. Oishi, I. Golynker, M. Panis, J. Zimering, S. Horiuchi, D. A. Hoagland, R. Møller, A. Ruiz, A. Kodra, J. B. Overdevest, P. D. Canoll, A. C. Borczuk, V. Chandar, Y. Bram, R. Schwartz, S. Lomvardas, V. Zachariou, B. R. TenOever, SARS-CoV-2 infection in hamsters and humans results in lasting and unique systemic perturbations post recovery. *Sci. Transl. Med.* (2022) (available at https://www.science.org/doi/full/10.1126/scitranslmed.abq3059).

33. L. Zanin, G. Saraceno, P. P. Panciani, G. Renisi, L. Signorini, K. Migliorati, M. M. Fontanella, SARS-CoV-2 can induce brain and spine demyelinating lesions. *Acta Neurochir. (Wien).* (2020), doi:10.1007/s00701-020-04374-x.

34. M. F. V. V. Aragão, M. C. Leal, O. Q. Cartaxo Filho, T. M. Fonseca, M. M. Valença, Anosmia in COVID-19 associated with injury to the olfactory bulbs evident on MRI. *Am. J. Neuroradiol.* (2020), doi:10.3174/ajnr.A6675.

35. F. Roy-Gash, D. M. Marine, D. Jean-Michel, V. Herve, B. Raphael, E. Nicolas, COVID-19-associated acute cerebral venous thrombosis: Clinical, CT, MRI and EEG features*Crit. Care* (2020), doi:10.1186/s13054-020-03131-x.

36. E. Carroll, A. Lewis, Catastrophic Intracranial Hemorrhage in Two Critically Ill Patients with COVID-19. *Neurocrit. Care* (2020), doi:10.1007/s12028-020-00993-5.

37. C. E. Fernandez, C. K. Franz, J. H. Ko, J. M. Walter, I. J. Koralnik, S. Ahlawat, S. Deshmukh, Imaging review of peripheral nerve injuries in patients with COVID-19*Radiology* (2021), doi:10.1148/radiol.2020203116.

38. R. M. C. Abrams, D. M. Simpson, A. Navis, N. Jette, L. Zhou, S. C. Shin, Small fiber neuropathy associated with SARS-CoV-2 infection. *Muscle and Nerve* (2021), doi:10.1002/mus.27458.

39. B. Neumann, M. L. Schmidbauer, K. Dimitriadis, S. Otto, B. Knier, W. D. Niesen, J. A. Hosp, A. Günther, S. Lindemann, G. Nagy, T. Steinberg, R. A. Linker, B. Hemmer, J. Bösel,

Cerebrospinal fluid findings in COVID-19 patients with neurological symptoms*J. Neurol. Sci.* (2020), doi:10.1016/j.jns.2020.117090.

40. G. Destras, A. Bal, V. Escuret, F. Morfin, B. Lina, L. Josset, Systematic SARS-CoV-2 screening in cerebrospinal fluid during the COVID-19 pandemic*The Lancet Microbe* (2020), doi:10.1016/S2666-5247(20)30066-5.

41. Y. H. Huang, D. Jiang, J. T. Huang, SARS-CoV-2 Detected in Cerebrospinal Fluid by PCR in a Case of COVID-19 Encephalitis*Brain. Behav. Immun.* (2020), doi:10.1016/j.bbi.2020.05.012.

42. R. B. Domingues, M. C. Mendes-Correa, F. B. V. de Moura Leite, E. C. Sabino, D. Z. Salarini, I. Claro, D. W. Santos, J. G. de Jesus, N. E. Ferreira, C. M. Romano, C. A. S. Soares, First case of SARS-COV-2 sequencing in cerebrospinal fluid of a patient with suspected demyelinating disease*J. Neurol.* (2020), doi:10.1007/s00415-020-09996-w.

43. Y. C. Li, W. Z. Bai, N. Hirano, T. Hayashida, T. Hashikawa, Coronavirus infection of rat dorsal root ganglia: Ultrastructural characterization of viral replication, transfer, and the early response of satellite cells. *Virus Res.* (2012), doi:10.1016/j.virusres.2011.12.021.

44. S. Perlman, G. Jacobsen, A. L. Olson, A. Afifi, Identification of the spinal cord as a major site of persistence during during chronic infection with a murine coronavirus. *Virology* (1990), doi:10.1016/0042-6822(90)90426-R.

45. R. Elliott, F. Li, I. Dragomir, M. M. W. Chua, B. D. Gregory, S. R. Weiss, Analysis of the Host Transcriptome from Demyelinating Spinal Cord of Murine Coronavirus-Infected Mice. *PLoS One* (2013), doi:10.1371/journal.pone.0075346.

46. O. O. Koyuncu, I. B. Hogue, L. W. Enquist, Virus infections in the nervous system*Cell Host Microbe* (2013), doi:10.1016/j.chom.2013.03.010.

47. S. Hosseini, E. Wilk, K. Michaelsen-Preusse, I. Gerhauser, W. Baumgärtner, R. Geffers, K. Schughart, M. Korte, Long-term neuroinflammation induced by influenza a virus infection and the impact on hippocampal neuron morphology and function. *J. Neurosci.* (2018), doi:10.1523/JNEUROSCI.1740-17.2018.

48. K. Dobrindt, D. A. Hoagland, C. Seah, B. Kassim, C. P. O'Shea, A. Murphy, M. Iskhakova, M. B. Fernando, S. K. Powell, P. J. M. Deans, B. Javidfar, C. Peter, R. Møller, S. A. Uhl, M. F. Garcia, M. Kimura, K. Iwasawa, J. F. Crary, D. N. Kotton, T. Takebe, L. M. Huckins, B. R. tenOever, S. Akbarian, K. J. Brennand, Common Genetic Variation in Humans Impacts In Vitro Susceptibility to SARS-CoV-2 Infection. *Stem Cell Reports* **16** (2021), doi:10.1016/j.stemcr.2021.02.010.

49. E. Song, C. Zhang, B. Israelow, A. Lu-Culligan, A. V. Prado, S. Skriabine, P. Lu, O. El Weizman, F. Liu, Y. Dai, K. Szigeti-Buck, Y. Yasumoto, G. Wang, C. Castaldi, J. Heltke, E. Ng, J. Wheeler, M. M. Alfajaro, E. Levavasseur, B. Fontes, N. G. Ravindra, D. van Dijk, S. Mane, M. Gunel, A. Ring, S. A. Jaffar Kazmi, K. Zhang, C. B. Wilen, T. L. Horvath, I. Plu, S. Haik, J. L. Thomas, A. Louvi, S. F. Farhadian, A. Huttner, D. Seilhean, N. Renier, K. Bilguvar, A. Iwasaki, Neuroinvasion of SARS-CoV-2 in human and mouse brain. *J. Exp. Med.* **218** (2021), doi:10.1084/JEM.20202135.

50. S. F. Sia, L. M. Yan, A. W. H. Chin, K. Fung, K. T. Choy, A. Y. L. Wong, P. Kaewpreedee, R. A. P. M. Perera, L. L. M. Poon, J. M. Nicholls, M. Peiris, H. L. Yen, Pathogenesis and transmission of SARS-CoV-2 in golden hamsters. *Nature* **583** (2020), doi:10.1038/s41586-020-2342-5.

903 51. D. J. Morales, D. J. Lenschow, The antiviral activities of ISG15*J. Mol. Biol.* **425** (2013),
904 doi:10.1016/j.jmb.2013.09.041.

905 52. P. Barragán-Iglesias, Ú. Franco-Enzástiga, V. Jeevakumar, S. Shiers, A. Wangzhou, V.
906 Granados-Soto, Z. T. Campbell, G. Dussor, T. J. Price, Type I interferons act directly on
907 nociceptors to produce pain sensitization: Implications for viral infection-induced pain. *J.*
908 *Neurosci.* **40** (2020), doi:10.1523/JNEUROSCI.3055-19.2020.

909 53. R. Eccles, Understanding the symptoms of the common cold and influenza*Lancet Infect.*
910 *Dis.* (2005), doi:10.1016/S1473-3099(05)70270-X.

911 54. M. Pietzner, E. Wheeler, J. Carrasco-Zanini, J. Raffler, N. D. Kerrison, E. Oerton, V. P. W.
912 Auyeung, J. Luan, C. Finan, J. P. Casas, R. Ostroff, S. A. Williams, G. Kastenmüller, M. Ralser,
913 E. R. Gamazon, N. J. Wareham, A. D. Hingorani, C. Langenberg, Genetic architecture of host
914 proteins involved in SARS-CoV-2 infection. *Nat. Commun.* **11** (2020), doi:10.1038/s41467-020-
915 19996-z.

916 55. A. Sharma, M. A. Pollett, G. W. Plant, A. R. Harvey, Changes in mRNA expression of class
917 3 semaphorins and their receptors in the adult rat retino-collicular system after unilateral optic
918 nerve injury. *Investig. Ophthalmol. Vis. Sci.* (2012), doi:10.1167/iovs.12-10799.

919 56. A. Verheyen, E. Peeraer, R. Nuydens, J. Dhondt, K. Poesen, I. Pintelon, A. Daniels, J. P.
920 Timmermans, T. Meert, P. Carmeliet, D. Lambrechts, Systemic anti-vascular endothelial growth
921 factor therapies induce a painful sensory neuropathy. *Brain* (2012), doi:10.1093/brain/aws145.

922 57. A. Moutal, L. F. Martin, L. Boinon, K. Gomez, D. Ran, Y. Zhou, H. J. Stratton, S. Cai, S. Luo,
923 K. B. Gonzalez, S. Perez-Miller, A. Patwardhan, M. M. Ibrahim, R. Khanna, SARS-CoV-2 spike
924 protein co-opts VEGF-A/neuropilin-1 receptor signaling to induce analgesia. *Pain* (2021),
925 doi:10.1097/j.pain.0000000000002097.

926 58. G. Taccola, P. J. Doyen, J. Damblon, N. Dingu, B. Ballarin, A. Steyaert, A. des Rieux, P.
927 Forget, E. Hermans, B. Bosier, R. Deumens, A new model of nerve injury in the rat reveals a
928 role of Regulator of G protein Signaling 4 in tactile hypersensitivity. *Exp. Neurol.* (2016),
929 doi:10.1016/j.expneurol.2016.09.008.

930 59. K. Prasad, F. Khatoon, S. Rashid, N. Ali, A. F. AlAsmari, M. Z. Ahmed, A. S. Alqahtani, M.
931 S. Alqahtani, V. Kumar, Targeting hub genes and pathways of innate immune response in
932 COVID-19: A network biology perspective. *Int. J. Biol. Macromol.* (2020),
933 doi:10.1016/j.ijbiomac.2020.06.228.

934 60. L. Provenzi, M. Fumagalli, G. Scotto di Minico, R. Giorda, F. Morandi, I. Sirgiovanni, P.
935 Schiavolin, F. Mosca, R. Borgatti, R. Montirosso, Pain-related increase in serotonin transporter
936 gene methylation associates with emotional regulation in 4.5-year-old preterm-born children.
937 *Acta Paediatr. Int. J. Paediatr.* (2020), doi:10.1111/apa.15077.

938 61. H. B. Raju, N. F. Tsinoremas, E. Capobianco, Emerging putative associations between non-
939 coding RNAs and protein-coding genes in neuropathic pain: Added value from reusing
940 microarray data. *Front. Neurol.* (2016), doi:10.3389/fneur.2016.00168.

941 62. X. Li, W. Wang, Q. Chen, Y. Zhou, L. Wang, H. Huang, Antinociceptive effects of IL-6R vs.
942 glucocorticoid receptors during rat hind paw inflammatory pain. *Neurosci. Lett.* (2020),
943 doi:10.1016/j.neulet.2020.135356.

944 63. D. Zhang, J. Y. Mou, F. Wang, J. Liu, X. Hu, CRNDE enhances neuropathic pain via
945 modulating miR-136/IL6R axis in CCI rat models. *J. Cell. Physiol.* (2019),

946 doi:10.1002/jcp.28790.

947 64. H. Wakabayashi, S. Kato, N. Nagao, G. Miyamura, Y. Naito, A. Sudo, Interleukin-6 Inhibitor
948 Suppresses Hyperalgesia Without Improvement in Osteoporosis in a Mouse Pain Model of
949 Osteoporosis. *Calcif. Tissue Int.* (2019), doi:10.1007/s00223-019-00521-4.

950 65. R. R. Ji, H. Baba, G. J. Brenner, C. J. Woolf, Nociceptive-specific activation of ERK in spinal
951 neurons contributes to pain hypersensitivity. *Nat. Neurosci.* (1999), doi:10.1038/16040.

952 66. A. Ciruela, A. K. Dixon, S. Bramwell, M. I. Gonzalez, R. D. Pinnock, K. Lee, Identification of
953 MEK1 as a novel target for the treatment of neuropathic pain. *Br. J. Pharmacol.* (2003),
954 doi:10.1038/sj.bjp.0705103.

955 67. S. Yamakita, Y. Horii, H. Takemura, Y. Matsuoka, A. Yamashita, Y. Yamaguchi, M.
956 Matsuda, T. Sawa, F. Amaya, Synergistic activation of ERK1/2 between A-fiber neurons and
957 glial cells in the DRG contributes to pain hypersensitivity after tissue injury. *Mol. Pain* (2018),
958 doi:10.1177/1744806918767508.

959 68. J. Zhang, J. Jiang, G. Bao, G. Xu, L. Wang, J. Chen, C. Chen, C. Wu, P. Xue, D. Xu, Y.
960 Sun, Z. Cui, Interaction between C/EBPβ and RUNX2 promotes apoptosis of chondrocytes
961 during human lumbar facet joint degeneration. *J. Mol. Histol.* (2020), doi:10.1007/s10735-020-
962 09891-8.

963 69. S. J. Rice, G. Aubourg, A. K. Sorial, D. Almarza, M. Tselepi, D. J. Deehan, L. N. Reynard, J.
964 Loughlin, Identification of a novel, methylation-dependent, RUNX2 regulatory region associated
965 with osteoarthritis risk. *Hum. Mol. Genet.* (2018), doi:10.1093/hmg/ddy257.

966 70. A. Tajar, J. McBeth, D. M. Lee, G. J. MacFarlane, I. T. Huhtaniemi, J. D. Finn, G. Bartfai, S.
967 Boonen, F. F. Casanueva, G. Forti, A. Giwercman, T. S. Han, K. Kula, F. Labrie, M. E. J. Lean,
968 N. Pendleton, M. Punab, A. J. Silman, D. Vanderschueren, T. W. O'Neill, F. C. W. Wu, Elevated
969 levels of gonadotrophins but not sex steroids are associated with musculoskeletal pain in
970 middle-aged and older European men. *Pain* (2011), doi:10.1016/j.pain.2011.01.048.

971 71. M. X. Xie, X. Y. Cao, W. A. Zeng, R. C. Lai, L. Guo, J. C. Wang, Y. Bin Xiao, X. Zhang, D.
972 Chen, X. G. Liu, X. L. Zhang, ATF4 selectively regulates heat nociception and contributes to
973 kinesin-mediated TRPM3 trafficking. *Nat. Commun.* (2021), doi:10.1038/s41467-021-21731-1.

974 72. L. Dong, B. B. Guarino, K. L. Jordan-Sciutto, B. A. Winkelstein, Activating transcription
975 factor 4, a mediator of the integrated stress response, is increased in the dorsal root ganglia
976 following painful facet joint distraction. *Neuroscience* (2011),
977 doi:10.1016/j.neuroscience.2011.07.059.

978 73. O. Q. Russe, C. V. Möser, K. L. Kynast, T. S. King, H. Stephan, G. Geisslinger, E.
979 Niederberger, Activation of the AMP-activated protein kinase reduces inflammatory nociception.
980 *J. Pain* (2013), doi:10.1016/j.jpain.2013.05.012.

981 74. T. S. King-Himmelreich, C. V. Möser, M. C. Wolters, J. Schmetzer, Y. Schreiber, N.
982 Ferreirós, O. Q. Russe, G. Geisslinger, E. Niederberger, AMPK contributes to aerobic exercise-
983 induced antinociception downstream of endocannabinoids. *Neuropharmacology* (2017),
984 doi:10.1016/j.neuropharm.2017.05.002.

985 75. G. Giaccone, P. Zatloukal, J. Roubec, K. Floor, J. Musil, M. Kuta, R. J. Van Klaveren, S.
986 Chaudhary, A. Gunther, S. Shamsili, Multicenter phase II trial of YM155, a small-molecule
987 suppressor of survivin, in patients with advanced, refractory, non-small-cell lung cancer. *J. Clin.*
988 *Oncol.* (2009), doi:10.1200/JCO.2008.21.1862.

76. M. R. Clemens, O. A. Gladkov, E. Gartner, V. Vladimirov, J. Crown, J. Steinberg, F. Jie, A. Keating, Phase II, multicenter, open-label, randomized study of YM155 plus docetaxel as first-line treatment in patients with HER2-negative metastatic breast cancer. *Breast Cancer Res. Treat.* (2015), doi:10.1007/s10549-014-3238-6.

77. A. W. Tolcher, D. I. Quinn, A. Ferrari, F. Ahmann, G. Giaccone, T. Drake, A. Keating, J. S. De Bono, A phase II study of YM155, a novel small-molecule suppressor of survivin, in castration-resistant taxane-pretreated prostate cancer. *Ann. Oncol.* (2012), doi:10.1093/annonc/mdr353.

78. T. Yamauchi, N. Nakamura, M. Hiramoto, M. Yuri, H. Yokota, M. Naitou, M. Takeuchi, K. Yamanaka, A. Kita, T. Nakahara, I. Kinoyama, A. Matsuhisa, N. Kaneko, H. Koutoku, M. Sasamata, M. Kobori, M. Katou, S. Tawara, S. Kawabata, K. Furuichi, Sepantronium Bromide (YM155) induces disruption of the ILF3/p54nrb complex, which is required for survivin expression. *Biochem. Biophys. Res. Commun.* (2012), doi:10.1016/j.bbrc.2012.07.103.

79. T. Nakahara, M. Takeuchi, I. Kinoyama, T. Minematsu, K. Shirasuna, A. Matsuhisa, A. Kita, F. Tominaga, K. Yamanaka, M. Kudoh, M. Sasamata, YM155, a novel small-molecule survivin suppressant, induces regression of established human hormone-refractory prostate tumor xenografts. *Cancer Res.* (2007), doi:10.1158/0008-5472.CAN-07-1343.

80. K. Avrampou, K. D. Pryce, A. Ramakrishnan, F. Sakloth, S. Gaspari, R. A. Serafini, V. Mitsi, C. Polizu, C. Swartz, B. Ligas, A. Richards, L. Shen, F. B. Carr, V. Zachariou, RGS4 Maintains Chronic Pain Symptoms in Rodent Models. *J. Neurosci.* **39**, 8291–8304 (2019).

81. E. Vachon-Presseau, P. Tétreault, B. Petre, L. Huang, S. E. Berger, S. Torbey, A. T. Baria, A. R. Mansour, J. A. Hashmi, J. W. Griffith, E. Comasco, T. J. Schnitzer, M. N. Baliki, A. V. Apkarian, Corticolimbic anatomical characteristics predetermine risk for chronic pain. *Brain* **139**, 1958–1970 (2016).

82. P. Muglia, F. Tozzi, N. W. Galwey, C. Francks, R. Upmanyu, X. Q. Kong, A. Antoniades, E. Domenici, J. Perry, S. Rothen, C. L. Vandeleur, V. Mooser, G. Waeber, P. Vollenweider, M. Preisig, S. Lucae, B. Müller-Myhsok, F. Holsboer, L. T. Middleton, A. D. Roses, Genome-wide association study of recurrent major depressive disorder in two European case-control cohorts. *Mol. Psychiatry* **15** (2010), doi:10.1038/mp.2008.131.

83. Y. Wang, L. Li, C. Xu, X. Cao, Z. Liu, N. Sun, A. Zhang, X. Li, K. Zhang, Polymorphism of ERK/PTPRR Genes in Major Depressive Disorder at Resting-State Brain Function. *Dev. Neuropsychol.* **42** (2017), doi:10.1080/87565641.2017.1306527.

84. M. Muriello, A. Y. Kim, K. Sondergaard Schatz, N. Beck, M. Gunay-Aygun, J. E. Hoover-Fong, Growth hormone deficiency, aortic dilation, and neurocognitive issues in Feingold syndrome 2. *Am. J. Med. Genet. Part A* **179** (2019), doi:10.1002/ajmg.a.61037.

85. H. Ganjavi, V. M. Siu, M. Speevak, P. A. MacDonald, A fourth case of Feingold syndrome type 2: Psychiatric presentation and management. *BMJ Case Rep.* **2014** (2014), doi:10.1136/bcr-2014-207501.

86. Y. Wen, X. Fan, H. Bu, L. Ma, C. Kong, C. Huang, Y. Xu, Downregulation of lncRNA FIRRE relieved the neuropathic pain of female mice by suppressing HMGB1 expression. *Mol. Cell. Biochem.* **476** (2021), doi:10.1007/s11010-020-03949-7.

87. K. Gómez, A. Sandoval, P. Barragán-Iglesias, V. Granados-Soto, R. Delgado-Lezama, R. Felix, R. González-Ramírez, Transcription Factor Sp1 Regulates the Expression of Calcium Channel α2δ-1 Subunit in Neuropathic Pain. *Neuroscience* (2019),

1033 doi:10.1016/j.neuroscience.2019.06.011.

1034 88. S. Li, F. Zhao, Q. Tang, C. Xi, J. He, Y. Wang, M. X. Zhu, Z. Cao, Sarco/endoplasmic
1035 reticulum Ca 2+ -ATPase 2b mediates oxidation-induced endoplasmic reticulum stress to
1036 regulate neuropathic pain . *Br. J. Pharmacol.* (2021), doi:10.1111/bph.15744.

1037 89. D. J. Kao, A. H. Li, J. C. Chen, R. S. Luo, Y. L. Chen, J. C. Lu, H. L. Wang, CC chemokine
1038 ligand 2 upregulates the current density and expression of TRPV1 channels and Nav1.8 sodium
1039 channels in dorsal root ganglion neurons. *J. Neuroinflammation* (2012), doi:10.1186/1742-2094-
1040 9-189.

1041 90. W. Xie, Z. Y. Tan, C. Barbosa, J. A. Strong, T. R. Cummins, J. M. Zhang, Upregulation of
1042 the sodium channel Na v β4 subunit and its contributions to mechanical hypersensitivity and
1043 neuronal hyperexcitability in a rat model of radicular pain induced by local dorsal root ganglion
1044 inflammation. *Pain* (2016), doi:10.1097/j.pain.0000000000000453.

1045 91. C. Barbosa, Z. Y. Tan, R. Wang, W. Xie, J. A. Strong, R. R. Patel, M. R. Vasko, J. M.
1046 Zhang, T. R. Cummins, Navβ4 regulates fast resurgent sodium currents and excitability in
1047 sensory neurons. *Mol. Pain* (2015), doi:10.1186/s12990-015-0063-9.

1048 92. A. Broyl, S. L. Corthals, J. L. M. Jongen, B. van der Holt, R. Kuiper, Y. de Knegt, M. van
1049 Duin, L. el Jarari, U. Bertsch, H. M. Lokhorst, B. G. Durie, H. Goldschmidt, P. Sonneveld,
1050 Mechanisms of peripheral neuropathy associated with bortezomib and vincristine in patients
1051 with newly diagnosed multiple myeloma: a prospective analysis of data from the HOVON-
1052 65/GMMG-HD4 trial. *Lancet Oncol.* (2010), doi:10.1016/S1470-2045(10)70206-0.

1053 93. N. Munawar, M. A. Oriowo, W. Masocha, Antihyperalgesic activities of endocannabinoids in
1054 a mouse model of antiretroviral-Induced neuropathic pain. *Front. Pharmacol.* (2017),
1055 doi:10.3389/fphar.2017.00136.

1056 94. R. Fu, Y. Tang, W. Li, Z. Ren, D. Li, J. Zheng, W. Zuo, X. Chen, Q. K. Zuo, K. L. Tam, Y.
1057 Zou, T. Bachmann, A. Bekker, J. H. Ye, Endocannabinoid signaling in the lateral habenula
1058 regulates pain and alcohol consumption. *Transl. Psychiatry* (2021), doi:10.1038/s41398-021-
1059 01337-3.

1060 95. Z. Hu, N. Deng, K. Liu, N. Zhou, Y. Sun, W. Zeng, CNTF-STAT3-IL-6 Axis Mediates
1061 Neuroinflammatory Cascade across Schwann Cell-Neuron-Microglia. *Cell Rep.* (2020),
1062 doi:10.1016/j.celrep.2020.107657.

1063 96. H. J. Chung, J. D. Kim, K. H. Kim, N. Y. Jeong, G protein-coupled receptor, family C, group
1064 5 (GPRC5B) downregulation in spinal cord neurons is involved in neuropathic pain. *Korean J.*
1065 *Anesthesiol.* (2014), doi:10.4097/kjae.2014.66.3.230.

1066 97. L. F. Ferrari, O. Bogen, N. Alessandri-Haber, E. Levine, R. W. Gear, J. D. Levine, Transient
1067 decrease in nociceptor GRK2 expression produces long-term enhancement in inflammatory
1068 pain. *Neuroscience* (2012), doi:10.1016/j.neuroscience.2012.07.004.

1069 98. N. Eijkelkamp, C. J. Heijnen, H. L. D. M. Willemen, R. Deumens, E. A. J. Joosten, W.
1070 Kleibeuker, I. J. M. Den Hartog, C. T. J. Van Velthoven, C. Nijboer, M. A. Nassar, G. W. Dorn, J.
1071 N. Wood, A. Kavelaars, GRK2: A novel cell-specific regulator of severity and duration of
1072 inflammatory pain. *J. Neurosci.* (2010), doi:10.1523/JNEUROSCI.5752-09.2010.

1073 99. M. Parisien, A. Samoshkin, S. N. Tansley, M. H. Piltonen, L. J. Martin, N. El-Hachem, C.
1074 Dagostino, M. Allegri, J. S. Mogil, A. Khoutorsky, L. Diatchenko, Genetic pathway analysis
1075 reveals a major role for extracellular matrix organization in inflammatory and neuropathic pain.

Pain (2019), doi:10.1097/j.pain.0000000000001471.

100. M. Imai, K. Iwatsuki-Horimoto, M. Hatta, S. Loeber, P. J. Halfmann, N. Nakajima, T. Watanabe, M. Ujie, K. Takahashi, M. Ito, S. Yamada, S. Fan, S. Chiba, M. Kuroda, L. Guan, K. Takada, T. Armbrust, A. Balogh, Y. Furusawa, M. Okuda, H. Ueki, A. Yasuhara, Y. Sakai-Tagawa, T. J. S. Lopes, M. Kiso, S. Yamayoshi, N. Kinoshita, N. Ohmagari, S. I. Hattori, M. Takeda, H. Mitsuya, F. Krammer, T. Suzuki, Y. Kawaoka, Syrian hamsters as a small animal model for SARS-CoV-2 infection and countermeasure development. *Proc. Natl. Acad. Sci. U. S. A.* **117** (2020), doi:10.1073/pnas.2009799117.

101. C. Muñoz-Fontela, W. E. Dowling, S. G. P. Funnell, P. S. Gsell, A. X. Riveros-Balta, R. A. Albrecht, H. Andersen, R. S. Baric, M. W. Carroll, M. Cavaleri, C. Qin, I. Crozier, K. Dallmeier, L. de Waal, E. de Wit, L. Delang, E. Dohm, W. P. Duprex, D. Falzarano, C. L. Finch, M. B. Frieman, B. S. Graham, L. E. Gralinski, K. Guilfoyle, B. L. Haagmans, G. A. Hamilton, A. L. Hartman, S. Herfst, S. J. F. Kaptein, W. B. Klimstra, I. Knezevic, P. R. Krause, J. H. Kuhn, R. Le Grand, M. G. Lewis, W. C. Liu, P. Maisonnasse, A. K. McElroy, V. Munster, N. Oreshkova, A. L. Rasmussen, J. Rocha-Pereira, B. Rockx, E. Rodríguez, T. F. Rogers, F. J. Salguero, M. Schotsaert, K. J. Stittelaar, H. J. Thibaut, C. Te Tseng, J. Vergara-Alert, M. Beer, T. Brasel, J. F. W. Chan, A. García-Sastre, J. Neyts, S. Perlman, D. S. Reed, J. A. Richt, C. J. Roy, J. Segalés, S. S. Vasan, A. M. Henao-Restrepo, D. H. Barouch, Animal models for COVID-19*Nature* **586** (2020), doi:10.1038/s41586-020-2787-6.

102. G. Gao, W. Li, S. Liu, D. Han, X. Yao, J. Jin, D. Han, W. Sun, X. Chen, The positive feedback loop between ILF3 and lncrna ILF3-AS1 promotes melanoma proliferation, migration, and invasion. *Cancer Manag. Res.* (2018), doi:10.2147/CMAR.S186777.

103. X. Yang, F. Lin, F. Gao, Up-regulated long non-coding RNA ILF3-AS1 indicates poor prognosis of nasopharyngeal carcinoma and promoted cell metastasis. *Int. J. Biol. Markers* (2020), doi:10.1177/1724600820955199.

104. X. hui Hu, J. Dai, H. lai Shang, Z. xue Zhao, Y. dong Hao, SP1-mediated upregulation of lncRNA ILF3-AS1 functions a ceRNA for miR-212 to contribute to osteosarcoma progression via modulation of SOX5. *Biochem. Biophys. Res. Commun.* (2019), doi:10.1016/j.bbrc.2019.02.110.

105. M. D. Sanna, N. Galeotti, The HDAC1/c-JUN complex is essential in the promotion of nerve injury-induced neuropathic pain through JNK signaling. *Eur. J. Pharmacol.* **825** (2018), doi:10.1016/j.ejphar.2018.02.034.

106. F. Sakloth, L. Manouras, K. Avrampou, V. Mitsi, R. A. Serafini, K. D. Pryce, V. Cogliani, O. Berton, M. Jarpe, V. Zachariou, HDAC6-selective inhibitors decrease nerve-injury and inflammation-associated mechanical hypersensitivity in mice. *Psychopharmacology (Berl).* **237** (2020), doi:10.1007/s00213-020-05525-9.

107. I. Vasileiou, I. Adamakis, E. Patsouris, S. Theocharis, Ephrins and pain*Expert Opin. Ther. Targets* (2013), doi:10.1517/14728222.2013.801456.

108. A. Leroux, B. Paiva dos Santos, J. Leng, H. Oliveira, J. Amédée, Sensory neurons from dorsal root ganglia regulate endothelial cell function in extracellular matrix remodelling. *Cell Commun. Signal.* (2020), doi:10.1186/s12964-020-00656-0.

109. M. E. Kerrisk, L. A. Cingolani, A. J. Koleske, in *Progress in Brain Research*, (2014).

110. N. N. Knezevic, A. Yekkirala, T. L. Yaksh, Basic/Translational Development of Forthcoming Opioid- and Nonopioid-Targeted Pain Therapeutics. *Anesth. Analg.* **125**, 1714–1732 (2017).

111. K. D. Pryce, H. J. Kang, F. Sakloth, Y. Liu, S. Khan, K. Toth, A. Kapoor, A. Nicolais, T. Che, L. Qin, F. Bertherat, H. Ü. Kaniskan, J. Jin, M. D. Cameron, B. L. Roth, V. Zachariou, M. Filizola, A promising chemical series of positive allosteric modulators of the μ-opioid receptor that enhance the antinociceptive efficacy of opioids but not their adverse effects. *Neuropharmacology* **195** (2021), doi:10.1016/j.neuropharm.2021.108673.

112. M. I. Love, W. Huber, S. Anders, Moderated estimation of fold change and dispersion for RNA-seq data with DESeq2. *Genome Biol.* (2014), doi:10.1186/s13059-014-0550-8.

113. E. Y. Chen, C. M. Tan, Y. Kou, Q. Duan, Z. Wang, G. V. Meirelles, N. R. Clark, A. Ma'ayan, Enrichr: Interactive and collaborative HTML5 gene list enrichment analysis tool. *BMC Bioinformatics* (2013), doi:10.1186/1471-2105-14-128.